University of Nottingham

Department of Physics and Astronomy

Masters Thesis

Towards speckle assisted holographic microscopy and trapping for cold atoms

Author:
David Collomb
4217758
Owen Murray
4206374

Supervisor:
Saijun Wu
Lucia Hackermuller

October 5, 2017

University of Nottingham
UK | CHINA | MALAYSIA

復旦大學
FUDAN UNIVERSITY

Abstract

Often overlooked as a cold atom imaging technique, holographic microscopy presents a number of potential benefits over currently used imaging techniques. To illustrate these benefits, and further develop the holographic technique towards higher resolutions, an innovate set-up that couples an aberration reducing lens array with a solid immersion lens has been developed. The phase retrieval of this system is investigated using various square, hexagonal and Penrose patterns. The known speckle sources from these patterns are also incorporated to allow the use of aberration correction techniques using Zernike functions. After applying numerical noise and error reduction techniques and upon application of Zernike functions, the images showed a minor correction, notably through first order corrections, and less so through the higher orders. Although the success in correction and noise removal is limited, the thesis presents a series of steps to improve future developments of the technique.

Complimenting holographic imaging, investigations have been undertaken into exciting new dipole trapping geometries using the Talbot and Montogomery effects for periodic and quasi-periodic patterns of holes and disk like scatterers. The resulting diffraction patterns have been shown as theoretically capable of trapping cold atoms. Analysis in this thesis surpasses the vastly studied para-axial limit. Beyond this regime, where perfect self-images are not always observed, is also studied. In addition to this, the change of angle of incidence is shown to shift the Talbot lengths. Of particular interest, the intricate diffraction generated by a quasi-periodic Penrose pattern is shown to produce hot spots at certain propagation planes. Maximum trap depths of over 1 mK for Rb 85 atoms at a distance within 20 μm away from the pattern.

Looking towards a future combination of holographic microscopy with Talbot/Montgomery trapping, a method using Penrose nanoparticle arrays is proposed to create intricate trapping lattices as a test bed of future improved holographic techniques.

Keywords: Holography, speckle noise, Talbot effect, cold atom imaging, solid immersion, Angular Spectrum, phase retrieval, lens aberration and optical dipole trapping.

Symbols

$E_{\pm}$	Dressed state energies	$\mathbf{E}_S$	Scattered wavefront
$\hbar$	Reduced Plancks constant	OD	Optical depth
Δ	Detuning from atomic resonance	ϕ	Phase
Ω	Rabi frequency	σ	Complex absorption cross-section
ω	Light angular frequency	x_{pix}	Pixel size
ω_0	Atomic resonance frequency	x_D	Lens diameter
δE	Stark shift potential	$\delta\lambda$	Linewidth
c	Speed of light	δ_{rel}	Relative noise
Γ	Spontaneous emission rate	∇	Del operator
I	Intensity	A	Spectrum
Z_T	Para-axial Talbot length	$\mathcal{F}(\mathcal{F})$	Fourier Transform (Inverse Fourier Transform)
Z_R	Non-para-axial Talbot length	M	Total grid size
k	Wavevector	W	Object size on grid
a	Lattice period	Δ_x	Sampling length
λ	Wavelength	fAC	Auto-correlation function
f_x, f_y	Spatial frequencies	$E^2_{F,n}$	Fourier domain error
n	Refractive index	$E^2_{O,n}$	Fourier domain error
$\mathbf{E}_R$	Probe wavefront field	T_{Dip}	Dipole temperature
$\mathbf{E}_0$	Probe wavefront amplitude	U_{Dip}	Dipole potential
		f_o	Opening fraction
		μ	Half the angular aperture

Abbreviations

MOT	Magneto-optical trap
BEC	Bose-einstein condensates
EMF	Electromagnetic field
FGB	Focussed gaussian beam
FM	Fluorescence microscopy
AI	Absorption imaging
PCI	Phase-contrast imaging
DGI	Dark-ground imaging
NA	Numerical aperture
CCD	Charge coupled
CMOS	Complementary metal-oxide-semiconductor device
AOM	Acoustic-optical modulator
DL	Diode laser
DE	Detector
OI	Optical Insulator
RVC	Rubidium vapour cell
SH	Shutter
CO	Collimator
PZT	Piezoelertic transducer
PBS	Polarization Beam splitter
SIL	Solid immersion lens
EBL	Electron beam lithography
SEM	Scanning electron image
ASM	Angular spectrum method
SCN	Spatially coherent noise
FDTD	Finite difference time domain
FT	Fourier transform
IFT	Inverse Fourier transform
DFT	Discrete Fourier transform
IDFT	Inverse discrete Fourier transform
FFT	Fast Fourier transform
IFFT	Inverse fast Fourier transform
GS	Gerchberg Saxton
ERGS	Error reduction Gerchberg Saxton

Contents

1 Introduction

The understanding of light and matter interactions has allowed researchers to explore and utilize the field of cold atom physics. Atoms can be reduced to sub-micro kelvin temperatures through a combination of techniques, starting with slowing through absorption and spontaneous emission of photons, followed by trapping with Magneto-optical traps (MOT) and an additional inhomogeneous magnetic field [1]. Loading into dipole traps for further cooling can obtain more exotic ensembles (for example Bose Einstein Condensates (BECs)). Atoms from a MOT may also be loaded into optical lattices to be used for the exploration of a wider range of physics. This includes studying condensed matter physics concepts, as well as looking at potential applications such as improved metrological techniques [2].

In-situ imaging of cold atom ensembles has enabled researchers to probe some of the most interesting concepts in atomic physics. Many imaging techniques, however, are destructive. Other limitations include limited sensitivities, imaging artefacts and difficulties imaging optical lattices with multiple state occupancies. Advancing cold atom ambitions, such as using and loading into atom chips or dense optical lattices for uses in quantum information, has brought a need for more effective imaging techniques [3].

Holographic imaging proposes numerous advantages over traditional imaging techniques. Notably, non-destructive imaging can be achieved with the simultaneous retrieval of probe phase shift and attenuation. Minimisation of aberrations is also possible using combinations of numerical and physical techniques. For cold atom research, however, holography still faces some challenges. These include speckle noise and the notorious twin and DC images.

This thesis presents research undertaken to improve holographic microscopy. Techniques have been implemented, as well as proposed, to achieve this aim. Progressing towards a higher numerical aperture can improve the resolution of the system. A source of known speckles can in fact be used to the advantage of holographic imaging by two ways. The first being to mitigate the disadvantage with lensed holographic microscopy, that being aberrations. Secondly, speckles can be used to generate a complex wavefront, allowing removal of the twin image. This thesis explores speckles to be used for both these purposes, however greater emphasis is placed on the removal of aberrations. Additionally, a method of creating more complex cold atom ensembles using periodic and quasi-periodic diffraction gratings has been investigated. In the future these may be used to test the strength of holographic microscopy, through the use of quasi-Talbot traps, with Penrose patterns.

2 Background

2.1 Dipole trapping

Many cold atom experiments involve the trapping of cold atoms within conservative potentials, arising as a result of the light shift. A simple understanding of the light shift, also known as the AC stark shift, can be gained considering a 2-level atom interacting with an electromagnetic field. It is found that this interaction generates a superposition of the two bare states, known

as the dressed states. The energy eigenvalues are found to be

$$E_{\pm} = \pm\hbar\frac{\sqrt{\Delta^2 + |\Omega|^2}}{2}. \tag{1}$$

with $\Delta = \omega - \omega_0$. The $\pm$ symbol refers to the two individual dressed states. For a very large detunings, $\Delta >> \Omega$, equation (1) can be expanded to show that

$$E_{\pm} = \pm\hbar\left(\frac{\Delta}{2} + \frac{|\Omega|^2}{4\Delta}\right). \tag{2}$$

Both dressed states are then shifted by the same factor,

$$\delta E = \pm\hbar\frac{|\Omega|^2}{4\Delta}, \tag{3}$$

denoting the Stark shift. Coupling this with spontaneous emission allows cooling and trapping of atomic samples.

Two important quantities need to be considered for cold atom trapping, the dipole potential and scattering rate, that determine how effective a trap is for a particular group of atoms. The scattering rate can be determined from [4]

$$\Gamma_{sc} = \frac{3\pi c^2}{2\hbar\omega_0^3}\frac{\omega}{\omega_0}^3\left(\frac{\Gamma}{\omega_0 - \omega} + \frac{\Gamma}{\omega_0 + \omega}\right)^2 I. \tag{4}$$

The dipole potential can be similarly defined by

$$U_{dip} = -\frac{3\pi c^2}{2\omega_0^3}\left(\frac{\Gamma}{\omega_0 - \omega} + \frac{\Gamma}{\omega_0 + \omega}\right) I. \tag{5}$$

Equations (4) and (5) highlight the importance of selecting appropriate combinations of detuning and intensity to achieve suitable trapping parameters. Generally, the scattering rate should be minimised. Increasing the detuning can accomplish this, but will negatively impact the trap depth. Intensity can subsequently be increased, meaning an appropriate trap depth is achieved alongside a reduced scattering rate.

With the dependence of (4) and (5) on the detuning, atoms experience a potential maxima or minima at the trapping beam's intensity maxima.

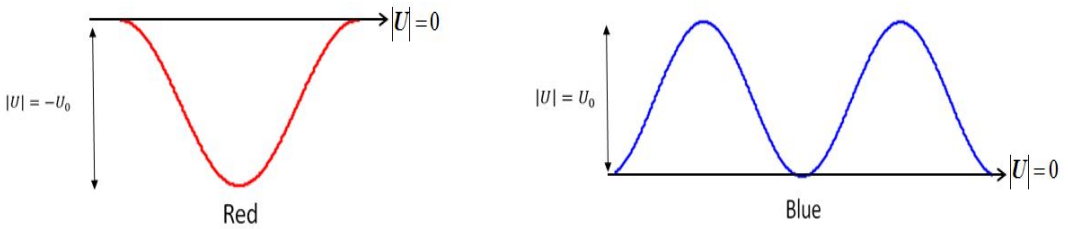

Figure 1: A trapping beam that is blue detuned will be repulsive to the atom at its intensity maxima, hence the atoms seeks to sit in the intensity minima, while a red detuned trap will be attractive to the atom at its intensity maxima.

Blue detuned based traps are usually box light structures, formed from beams, that atoms 'sit in'. Trapping is then typically performed vertically through gravity [5]. The most simple case of a red detuned trap, being a focused Gaussian beam trap, has a potential minimum at the centre of the beam that coincides with the intensity maximum, This is shown in the figure below [6].

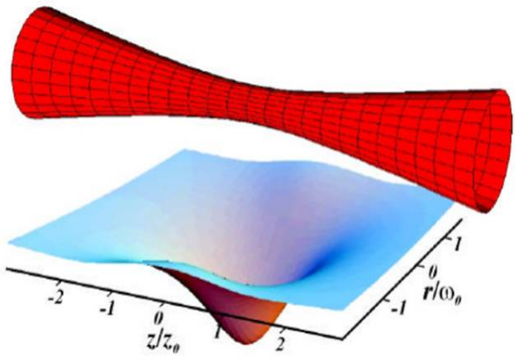

Figure 2: A schematic of the simplest form of dipole trap, the focussed Gaussian beam. This trap has tight radial confinement, but weak axial confinement. Atoms then tend to spread out in the axial direction. Atoms trapped of the focused beam trap tend then to resemble a line of atoms

Other forms of dipole traps such as crossed beam traps, often used for evaporative cooling, also exist [4].

Dipole forces can be used to form even more complex trapping potentials, such as optical lattices. Dense atomic ensembles on the order of 10^{12} atoms/cm^3 can be obtained, increasing the demand on cold atom imaging techniques [4]. Due to rising interest in optical lattices for cold atom applications, notably the simulation of condensed matter physics, it is of particular importance that imaging techniques are able to extract high quality information [7].

2.2 The Talbot effect

Illumination of a diffraction grating results in repeated 'self-images' of the grating, produced at regular intervals known as the Talbot length Z_T. This near-field diffraction effect was discovered by Talbot in 1836, although initial investigations used the para-axial approximation. In this limit the wavevector is considered much greater than extensions in the 2 perpendicular directions (for example $k >> k_x^2 + k_y^2$). Under this assumption the Talbot length is very simple and generates complete self-imaging. This effect, however, is not limited by this approximation and length scales can be determined that go beyond this limit. Within this regime, however, complete revivals are not guaranteed, and instead the focal points depend on the wave indices in reciprocal space. Similar effects of self-imaging can also be observed at fractional, rational multiples of Z_T.

As investigated by [8], irrational fractions of the Talbot length create even more interesting structures. These are found to be purely fractal functions. Mapping this in the 1D case

generates an incredibly intricate pattern, commonly referred to as the 'Talbot carpet',

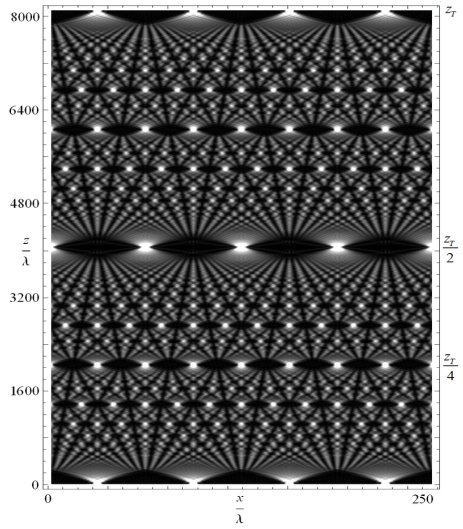

Figure 3: An example of a Talbot design where the bottom of the y axis along the x axis is the diffraction grating. The top is one Talbot length where the grating structure is recreated. At a quarter of the length, the image is halved in size with half of the grating period. At an eighth, another halving occurs, and so forth.

Lateral periodicity is key for the Talbot effect, and so is not limited to a single pattern type. For example, a periodic hexagonal pattern will be repeated at particular Talbot lengths, albeit different to a simple square lattice. [9]. Non-periodic gratings, such as Penrose patterns, can also form revival patterns. This arises as a results of the Montgomery effect, and even more intriguing, repeating images [10] can be observed.

Various patterns and potentially tighter lattice site periods may allow formation of more intricate optical lattices. Atoms could be trapped at integer or particular fractional Talbot lengths, and previous investigations have been undertaken for different cold atom physics experiments. An example includes the cooling of atoms[11]. Another study explores a 5x5 square array created using 25 co-propagating Gaussian laser beams [12]. Beam intensity was found to fall off with distance from the grating, where at the full length the intensity was four times smaller than the half length. The potential depth at the half length for Rubidium atoms was shown to be 91μK, hence demonstrating its feasibility for atom trapping [12].

Talbot trapping has been previously discussed in scientific literature for both square and triangular periodic patterns. Simulating new, more intricate, patterns could allow exploration of new avenues for cold atom trapping. This thesis explores the Penrose pattern as a potential candidate, and investigates whether diffraction 'hot spots' can form suitable trapping sites [13]. Although seemingly opaque, plates hosting the diffraction grating hold the ability to transmit a small percentage of incident light due to material imperfections [14]. To minimize costs, in addition to this transmission, light incident at 45 degrees to the array can implemented, from within a glass hemisphere, onto its flat edge. These particles act as an array of scatterers. Effects similar to having holes in an opaque plate would then produced, but with reduced transmission.

2.2.1 Square Array

The square array is the simplest 2D mask that may be used for observing the Talbot effect. Assuming a perfectly periodic array, a Fourier deconvolution can be performed to represent a diffracted wave at a position z, from interaction with a mask at z=0. Interaction of the wave and mask shown in figure 4 produces a diffracted wave that can be written mathematically as

$$\psi(x,y,z) = \sum_{n=-\infty}^{\infty} \sum_{m=-\infty}^{\infty} A_{n,m} \exp\left(i(k_x x + k_y y)\right) \exp\left(ik_z z\right). \tag{6}$$

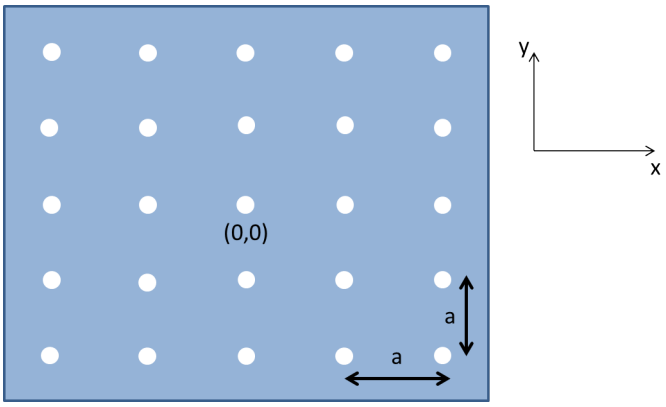

Figure 4: Illustration of a square array mask, with a lattice period of a in both the x and y directions. Interaction between the light and mask cause the light to be diffracted through the holes.

The important quantity for Talbot self-imaging is the additional phase factor due to propagation, written as

$$\exp\left(ik_z z\right) = \exp\left(izk\sqrt{1-\left(\frac{k_x}{k}\right)^2-\left(\frac{k_y}{k}\right)^2}\right), \tag{7}$$

for $k = \left(\frac{2\pi n}{a}, \frac{2\pi m}{a}, k_z^{n,m}\right)$. Under the para-axial limit, $\frac{a}{\lambda} \gg 1$, (7) can be Taylor expanded so that

$$\exp\left(ik_z z\right) \propto \exp\left(-i\pi(n^2+m^2)\frac{z}{Z_T}\right), \tag{8}$$

ignoring a constant, with

$$Z_T = \frac{a^2}{\lambda}. \tag{9}$$

In the case that $z = sZ_T$, for s a positive integer, if s is even then the exponent is a multiple of 2π as n^2+m^2 is an integer. The distribution at z=0 is then recovered, hence the name self-image. For s=odd, the exponent is a multiple of π and the original array is again recovered, albeit shifted by half of the grating period[15].

The fractional Talbot effect appears as revivals occurring at fractional Talbot lengths, $z = \frac{p}{q} Z_{T,Sq}$ with p and q being co-prime integers and p<q. It has been shown by [8] and [16]

that p and q play important roles in Talbot diffraction patterns. In summary, p determines the relative positions of the self images, while the period and size is multiplied by the factor $\frac{1}{q}$. For $z = \frac{1}{2}Z_{T,Sq}$ the pattern period and size is halved, for $z = \frac{1}{3}Z_{T,Sq}$ or $z = \frac{2}{3}Z_{T,Sq}$ they are reduced to a third, and so on. This occurs due to the fractional planes comprising of superposition's of multiple copies of the pattern. The number of superimposed copies is given by the value q. Particular importance is placed on the planes defined by $\frac{p_m}{q_m}$ for m$\rightarrow \infty$.

A significant amount of research uses the para-axial assumption. If, however, the para-axial limit is not held then the phase exponent cannot be Taylor expanded. In this case another method of determining the self-image distance is needed. A necessary condition for constructive interference, required for self-imaging, is that all the plane waves must be in phase. Choosing the centre frequency as a reference, this condition is represented by

$$\exp\left(ik_z^{n.m}Z_{R,Sq}\right) = \exp\left(ik_z^{0.0}Z_{R,Sq}\right), \tag{10}$$

and the new Talbot length is given by

$$Z_{R,Sq} = \frac{\lambda}{1 - \sqrt{1 - (n^2 + m^2)\left(\frac{\lambda}{a}\right)^2}}. \tag{11}$$

No perfect self-image distance then exists. Instead it depends on the individual plane wave (n,m), although it is found experimentally that diffraction patterns do not deviate significantly from the initial structure at certain Z_R[15]. It is important then to consider the parameters of the system when attempting to observe Talbot images, or intensity spots for cold atom trapping.

For incident light not normal to the surface, the Talbot length should be multiplied by a factor of $\frac{1}{cos\theta}$, where theta is the angle between the propagation direction and the axis normal to the pattern. As θ is increased, however, the para-axial limit begins to break. At 45 degrees to the surface, the para-axial approximation of $k^2 \gg k_x^2 + k_y^2$, or rather $k_z^2 \gg k_x^2 + k_y^2$, cannot hold. Both sides must actually be equal. The para-axial approximation then cannot be used, and only (11) should be considered.

2.2.2 Hexagonal Array

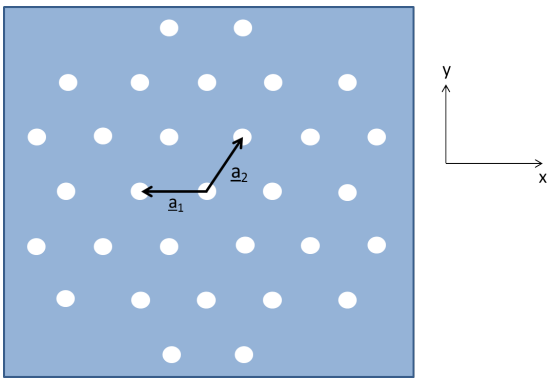

Figure 5: Illustration of a hexagonal array mask. The unit vectors for the array are given by $\underline{a}_1$ and $\underline{a}_1$. The lattice period in the x direction is the same as for the square array in figure 4.

The difference between this and the square array is that the unit vectors have different definitions, and so affects the reciprocal lattice. For the mask in figure 5, the two wave vector components are found to be

$$\underline{k}_1 = \frac{2\pi n}{a}\left(\underline{i} - \frac{1}{\sqrt{3}}\underline{j}\right) \tag{12}$$

and

$$\underline{k}_2 = \frac{4\pi m a\sqrt{3}\underline{j}}{.} \tag{13}$$

where the lattice period in the x-direction is the same as for the square lattice. Substituting these expressions into (6), the Talbot length for the Hexagonal array under the para-axial approximation is

$$Z_{T,Hex} = \frac{3a^2}{2\lambda}. \tag{14}$$

Beyond the para-axial limit a similar expression to equation (11) is obtained, given by

$$Z_{R,Hex} = \frac{\lambda}{1 - \sqrt{1 - \frac{4}{3}\left(\frac{\lambda}{a}\right)^2\{n^2 + m^2\}}}.. \tag{15}$$

For light propagation that is not normal to the surface, the Talbot length should vary in the same manner as described for the square pattern.

2.2.3 Penrose Pattern

Talbot self-imaging can only be applied to periodic objects. In 1967, W. Duane Montgomery found that lateral periodicity was not actually necessary[17]. Equation (6) can be rearranged into

$$\exp\left(ik_z z\right) = \exp\left(iz\frac{2\pi}{\lambda}\sqrt{1 - \lambda^2\left(f_x^2 + f_y^2\right)}\right), \tag{16}$$

where $f_x = \frac{n}{a_x}$ and $f_y = \frac{m}{a_y}$, for associated lattice periods a_x and a_y. Self-imaging then occurs for the condition

$$\frac{z}{\lambda}\sqrt{1 - \lambda\left(f_x^2 + f_y^2\right)} = m', \tag{17}$$

where m' is an integer depending generally on the spatial frequency (i.e. m' = m(f)). Assuming the spectrum is not zero for $f = 0$, it can be shown that [17]

$$f^2 + \left(\frac{m(f)^2}{z^2} - \frac{1}{\lambda^2}\right)^2 = \left(\frac{1}{\lambda}\right)^2 \tag{18}$$

for $f^2 = f_x^2 + f_y^2$ and m(f) = m'(0) - m'(f). This describes a circle of radius $\frac{1}{\lambda}$, centred at $\frac{1}{\lambda}$, in the $|f| - \frac{m}{z}$ plane. Self-imaging then occurs for all points coinciding with a particular set of circles, or rings, in reciprocal space. These are known as Montgomery rings.

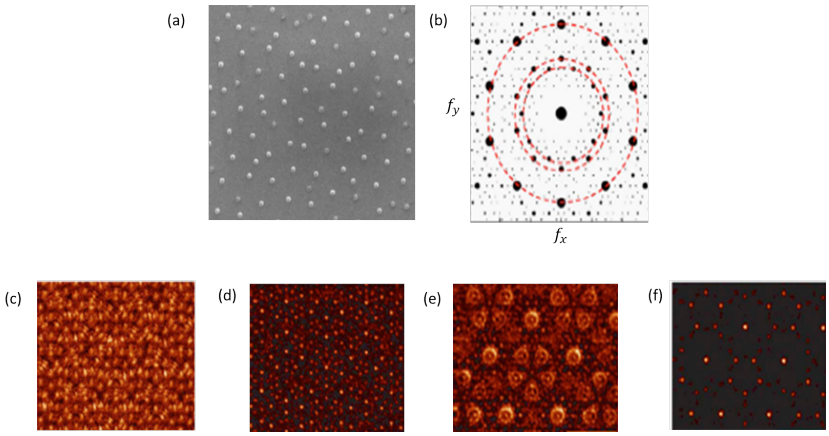

Figure 6: Illustrations of the occurrence of hot-spots, when illuminating a Penrose pattern, due to the overlap between reciprocal lattice points and the Montgomery rings. a shows the fabricated quasi-crystal pattern on a 20 x 20 μm grid, with an associated reciprocal lattice detailed in b.The spot diameter scales with the magnitude of the spectral component. The rings in b represent the Montgomery rings that coincide with some of the reciprocal lattice points.c-f represent the changing diffraction pattern observed when translating away from the Pattern, with illumination of wavelength 500nm. The distances away from the pattern are 0.3μm, 10μm, 19μm and 26μm going left to right.

Applying this to quasi-periodic objects, figure 6(a) can be studied [18] where a Penrose pattern was fabricated using the algorithm described in [19]. Figure 6(b) illustrates the corresponding reciprocal lattice. Montgomery rings are represented by the red circles, governing the revival distribution for particular z-planes. Quasi-periodic revivals can be understood as superpositions of large number s of partial reconstructions. Importantly, there exist some distances at which well-defined foci appear. These 'hot-spots' are sparsely distributed points, harvesting light from a large numbers of holes and resulting in high intensity. Figures 6(c)-(f) show the evolution of these revivals. For (c), close to the plate, the wave distribution is concentrated around the holes. At (b) a set of hot-spots begin to appear. Moving to (e) causes the pattern to change significantly, where the image becomes blurred and de-focused due to waves focussing at different positions. Finally, at (f), the bright spots then re-emerge, but with a different distribution than at (b).

A wide range of patterns can then exhibit this revival phenomenon due to this general effect, regraded as the Montgomery effect. The Talbot effect is merely a small part of this wider phenomenon, applying only to periodic structures.

2.3 Phase shift, Optical Depth and column density

When seeking to image cold atom systems, there are two important quantities that are generally measured. These are the phase shift and optical depth. When interacting with a cold atom sample the probe light's phase may be shifted, while the optical depth is a dimensionless parameter quantifying the ability of a sample to absorb passing light. The probing field in a

vacuum can be defined by

$$\mathbf{E_r} = \mathbf{E_0} e^{i(kz-\omega t)}, \tag{19}$$

where z is the propagation distance. A wave travelling through a sample with non-uniform refractive index can be expressed by

$$\mathbf{E_r} + \mathbf{E_s} = \mathbf{E_0} e^{i(k\int n_{Re} dz - wt)} e^{-k\int n_{Im} dz}, \tag{20}$$

where n_{Im} and n_{Re} indicate the imaginary and real refractive indexes respectively. Re-arranging for the scattered wavefront gives

$$\mathbf{E_s} = \mathbf{E_r}(e^{-\frac{OD}{2}+i\phi} - 1). \tag{21}$$

This is an important equation when discussing the retrieval of information via holography. Of particular importance, these quantities allow a determination of the column density, defined by the number of units of matter seen along a line of sight. Mathematically, the column density is defined as the integral of the number density along a direction. In terms of the previous quantities, the column density can be determined from

$$\phi = \int (n_{Re} - 1) dz = \frac{p_c \sigma_{Re}}{2} \tag{22}$$

or

$$OD = 2k \int n_{Im} dz = p_c \sigma_{Im}, \tag{23}$$

where $\sigma = \sigma_{Re} + \sigma_{Im}$.

2.4 Holographic microscopy

Holography, as a concept dates, back to Dennis Gabor in 1949, where it was initially considered as a method to avoid aberrations in electron microscopy [20]. By illuminating a sample at z_0 away from a source, with a known reference field $\mathbf{E_f}$, this interaction generates a secondary wave, $\mathbf{E_s}$. Digital holography can then be split into two steps, the first being the retrieval of the hologram, $\mathbf{H}$. This hologram is defined by

$$\mathbf{H} = |\mathbf{E_r} + \mathbf{E_s}|^2 = |\mathbf{E_r}|^2 + \mathbf{E_r^* E_s} + \mathbf{E_r E_s^*} + |\mathbf{E_s}|^2, \tag{24}$$

and is typically recorded with a CCD or CMOS detector. The first term is the far-field reference intensity, obtained simply by recording the hologram without a sample. From left to right the remaining terms are the real image, twin image and DC images respectively.

Secondly, the extraction of $\mathbf{E_s}$ via a numerical process - see section (2.5). The twin image, a virtual image located an equal distance from the source as the object but on the opposite side, and the DC image present initial downfalls of holography. A variety of techniques, however, can be implemented to solve these issues, including phase shifting holography, subtraction based and iterative phase retrieval based techniques [21, 22].

Various in-focus imaging methods can be applied to cold atoms, divided into 2 additional categories. These include the incoherent technique of florescence microscopy, and coherent

techniques of absorption, phase-contrast and dark-ground imaging. While these methods can be successfully used in cold atom experiments, there are a number of flaws associated with each technique.

Fluorescence imaging involves a very simple set-up but lacks the ability to accurately record single atoms in high density samples. Holography can improve upon this as the shot noise is independent of the atom number. More accurate single atom imaging is then possible. This is also a resonant technique and poses a risk of florescence re-absorption. Both this and the coherent technique of absorption imaging share some common features, an example being difficulties associated with imaging optical lattices with multiples site occupancies. In this case atoms can be lost in pairs due to both being resonant techniques. Holographic microscopy improves upon this because it is an off-resonant technique. Holography is also not limited by the Beer-Lambert law, used for intensity in florescence and absorption imaging, meaning it is an improved imaging method for dense samples where this law breaks down.

In particular for absorption imaging, holography improves upon situations where $OD >> 1$. Such a situation can lead to a blocking out of the probe beam, making it difficult to retrieve any useful information. Holography, being off resonant, allows the detuning to be increased. Even dense atomic samples can then be imaged.

Phase-contrast and dark-ground imaging are, like holography, off-resonant techniques. Being in-focus techniques, they can be improved upon with holography. PCI uses a phase plate to phase shift the scattered light from a sample to form an interference pattern with the probe light. Detection of this interference pattern then allows recovery of useful information in the phase. DGI uses a mask to cut out the probe light entirely. Both methods, however, face the same problem. Recovery of information, after incorporating the plate or mask, assumes perfect alignment of the beams focussed by a lens. This is not the case. Imperfect focussing results in imaging artefacts. These arise as a result of parts of probe light phase shifted in PCI, and parts of the probe/ scattered light that is unblocked/blocked in DGI. Additionally, the lenses in these techniques need to collimate and focus the scattered and probe light simultaneously. A single lens cannot achieve this perfectly meaning unwanted aberrations are inevitable, making high NA imaging with these techniques very difficult. Holographic microscopy improves upon these limitations because it uses a very simple set-up. Only the interference pattern is required to form the hologram, meaning it can be potentially aberration free. When using the lenses to increase the NA of the system, these distortions can be corrected for with known aberration correction techniques. Higher quality images are then possible.

A major advantage of the holographic technique, compared to both incoherent and coherent methods, is that it can grant 3D fields of view. Because these methods record 'slices' of the column density, multiple images are required for an estimation of the 3D image. Holography instead records interference at diffraction planes and so, with the reconstructed image, different planes can be focussed on. This 3D image can be acquired with just a single shot.

This section explores some of the methods for digital holography and looks at current hurdles to be overcome for application to cold atom imaging.

2.4.1 In-line holography

A general set-up for in-line holographic imaging is shown in figure 7, where a sample is illuminated at a distance z_0 away from a point source

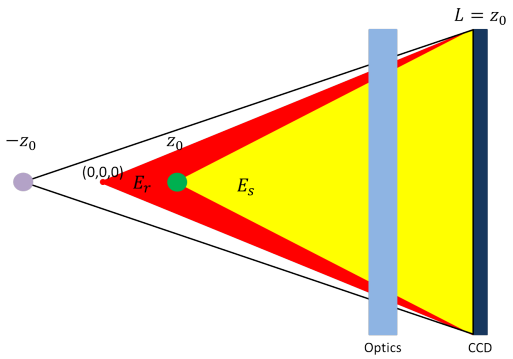

Figure 7: An in-line holographic imaging set-up, where the interaction between the probe light, $\mathbf{E_r}$, and the object results in the scattered wavefront $\mathbf{E_s}$.

and the resultant interference pattern is recorded by the CCD translated to a diffraction plane. A hologram without the object is given simply by $\mathbf{H_0} = |\mathbf{E}_r|^2$, meaning the scattered wavefront can be defined by

$$\mathbf{E_H} = \frac{\mathbf{H} - \mathbf{H_0}}{\mathbf{E}_r^*} = \mathbf{E}_s + \frac{\mathbf{E}_r \mathbf{E}_s^*}{\mathbf{E}_r^*} + \frac{|\mathbf{E}_s|^2}{\mathbf{E}_r^*}. \tag{25}$$

Object and twin images are located at $z = \pm z_0$, while the DC term is focussed at $z = 0$. Distortions then arise as both are in-line with the object image.

One key advantage of the in-line holographic technique is that the set-up is very similar to AI, only the CCD is translated to a diffraction plane. This characterises the holographic techniques as an out-of-focus technique. Simply converting an AI system, however, can introduce unwanted aberrations into the image given that holographic techniques can be used without lenses. Standard holographic set-ups are then ideal for high NA systems without reduced depth of view. Multiple objects can then be imaged, at unknown distances, with a single shot. Distortions do arise as a result of the twin and DC images . Effective removal techniques are required to improve the quality of numerically reconstructed image.

In order to solve the twin image problem a different set-up can used, known as off-axis holographic microscopy. A key difference for this technique is that the probe beam is split in two, where one remains in the probe path to interact with the sample, and the second is directed around. The two beams are then recombined at the detector with a relative angle. Interference between light from these two paths then generates the hologram from which the probe and scattered wavefront can be extracted, and later used for reconstruction. In this case the real and twin images are spatially separated, at their associated focal planes. Its pitfalls, and reasons for infrequent use, include a more complex set-up with additional optical components. Increased speckle noise and aberrations are then introduced into the images. With standard CCDs it is also difficult to achieve high resolutions with high NA set-ups.

Atomic optical properties can be recovered from known scattered and reference fields. In the sample's focal, the OD and phase shift are given by,

$$OD = 2Re(ln(1 + \frac{\mathbf{E}_s}{\mathbf{E}_r})), \tag{26}$$

$$\phi = Im(ln(1 + \frac{\mathbf{E}_s}{\mathbf{E}_r})). \tag{27}$$

The column density can also be obtained from the absorption cross section, and using the equation from section 2.1.3. Summing the column density over the split pixels,

$$N = \sum_{Pixels} \rho_c x_{pix,T}^2, \tag{28}$$

the atom number can be determined. Here, $x_{pix,T} = x_{pix}/T$, where T is the number of sub pixels each initial camera pixel is split into [23](see section 2.4.2).

2.4.2 Resolution

Resolution is an important quantity in imaging and defines the the smallest resolvable features, or the minimum spacing between two points for both to remain resolvable. Definitions also vary for incoherent and coherent imaging methods.

For incoherent techniques, e.g. Florescence imaging, the lateral resolution, $R_{lat} = \frac{2\pi}{|\underline{k}_{lat}|}$, can be defined by

$$R_{lat} = \frac{\lambda}{2n \sin\theta} \tag{29}$$

with an imaging wavelength of λ.

Coherent techniques are sensitive to the scattered wavefront. Resolution is then determined from the resultant spatial frequency, opposed to the intensity. In holographic reconstruction a ray extending from the hologram edge, and focussed to form the image, will have $|\underline{k}_{lat}| = n|\underline{k}| \sin\theta$. Lateral and depth resolutions will then be given by

$$R_{lat} = \frac{\lambda}{n \sin\theta} \tag{30}$$

$$R_{dep} = \frac{\lambda}{n\,(1 - \cos\theta)} \tag{31}$$

respectively. For an object on the central imaging axis, depicted in figure 8, the NA can be defined as

$$NA_i = n \sin\theta = n \sin\left[\tan^{-1}\left(\frac{x_D}{2(L - z_0)}\right)\right]. \tag{32}$$

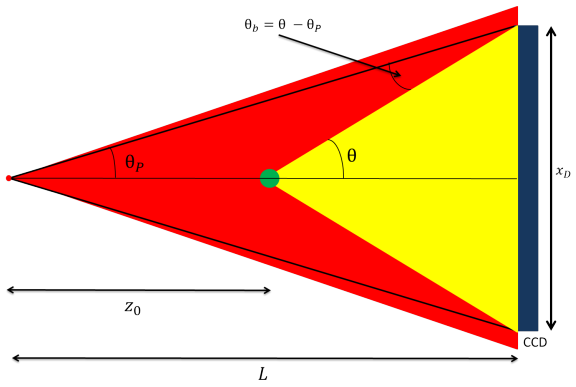

Figure 8: Diagram showing an in-line holographic imaging setup, with annotations of angles for the calculation of the numerical aperture.

From the Whittaker-Shannon sampling theorem, however, the fringe period of the interference pattern must be larger than at least two pixels, or $\frac{\lambda}{\sin\theta_b} \leq 2x_{pix}$. Digitally recovered images will then be free of aliasing. This condition places a maximum value on the achievable NA that, for the given geometry, is defined by

$$NA_{max} = n\sin\left(\theta_b + \theta_p\right) = n\sin\left(\sin^{-1}\left(\frac{\lambda}{2x_{pix}}\right) + \tan^{-1}\left(\frac{x_D}{2(L+z_0)}\right)\right). \tag{33}$$

Limited values of z_0 then exist for which aliasing will not occur, up to $z_{0,max}$ when $NA_i = NA_{max}$. Making small angle approximations with $z_0 << L$ and $x_D << 2L$, for the object in front of the source, the maximum object-source separation is approximated as

$$z_{0,max} \approx \frac{\lambda L^2}{2x_D x_{pix}}. \tag{34}$$

When $z_0 > z_{0,max}$ the detector will be unable to resolve the interference fringes, meaning the NA will be undefined and aliasing is introduced.

An additional limit to consider is the pixel limit, referring directly to the recording instrument. When recording the interference pattern, fringes may not be directly observable but this does not mean the image is poor. The camera pixels may be too large to resolve smaller features and, when propagating the hologram back to the image plane, resultant images will be limited by this pixel size. It is possible, however, to overcome this. In a procedure known as pixel splitting, the grid making up the image is split into a larger number of pixels (i.e. interpolation of signal onto a finer grid). Resolution of holographic techniques can then be improved, possibly preventing aliasing (review section 2.5.2 for direct application to holographic reconstruction).

2.4.3 Speckle noise

Speckle noise is a granular noise resulting from surface or optical defects on the scale of light wavelengths. Random path length differences between coherent photons are then produced that interfere at the detector, modulating the measured intensity.

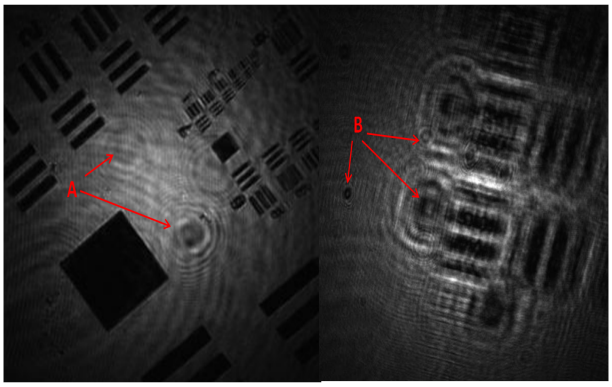

Figure 9: Example of speckle noise during image retrieval of an optics bench calibration pattern. Example speckle artefacts are highlighted at A and B.

Holography is victim to this noise, introduced as a result of locking to the narrow atomic transitions. It is one of its main obstacles to overcome before becoming a reliable technique for cold atom imaging. The coherence of a laser is given by

$$L_{coh} = \frac{\lambda^2}{\delta\lambda}. \tag{35}$$

Light of low coherence will then less likely form speckles because individual wavelengths, with different dimensions, will normally average out [24].

Speckle noise has been avoided in other techniques using multi-coloured or short-coherent length lasers to average out speckle interferences [25]. Phase plates have also been introduced to average out time-varying speckle pattern. although this is difficult in cold atom experiments due to long integration times [26]. Outside of cold atom research, the linewidth in equation (35) can be increased to avoid the effect of speckle noise [7]. The "greedy algorithm", where speckles are included one by one into the wavefront with calculations, can also be implemented to account for speckle noise [23].

Given that current holographic techniques require lenses, and the desire for expansion of cold atom imaging to atom chips, being able to account for speckle has become a priority for further development [23].

2.4.4 Shot noise

Shot noise has a number of slightly different definitions depending on the particular area of application. In optics, where photons from a sample are collected by a sensor, the shot noise is described by the fluctuation in the detected photon number. Fluctuations occur due to the discretisation of the electromagnetic energy. Detector efficiency is then quantified by the effective shot noise level from the random conversion of photons into an electronic signal.

For photons in squeezed coherent states, fluctuations of the photon count can be less than the square root of the photon expectation number. Other sources of noise, such as background and readout noise, also become less important when the intensity is increased. Increasing the

intensity further can make the photon shot noise dominant, even approaching photon noise limited. Only a single noise then need be corrected for.

When taking a single image, the relative noise is given by

$$\delta_{rel} = \frac{\delta I_1}{I_1} \tag{36}$$

for the noise in the intensity, δI_1, and the measured intensity, I_1, on the first pixel of the sensor. If the average of N images is taken, the relative noise is approximated by

$$\delta_{rel,N} = \frac{1}{\sqrt{N}} \frac{\delta I_1}{I_1}. \tag{37}$$

Relative noise is then reduced by a factor of $\sqrt{N}$. Taking the average of a greater number of images then reduces the effects of shot noise in the image.

2.5 Algorithms for wavefront propagation and retrieval

The task in digital holography is to identify the scattered wavefront, $\mathbf{E}_s$, from interference with a known probe field $\mathbf{E}_r$. Operating as an imaging technique, phase retrieval is crucial. In doing this it is possible to generate an in-focus image at the focal plane from estimations at the diffraction plane.

2.5.1 Angular Spectrum algorithm

While various methods of obtaining the scattered wavefront exist, a precise method in many cases is the angular spectrum method (ASM). The Helmholtz equation is defined by

$$\left(\nabla^2 + k^2\right) \mathbf{E}(x, y, z) = 0 \tag{38}$$

for a complex field $\mathbf{E}(x, y, z)$. This field can be considered of the form $\mathbf{E}(x, y, z) = \mathbf{E}(x, y)e^{ik_z z}$, where $\mathbf{k}^2 = k_x^2 + k_y^2 + k_z^2$. If $\mathbf{E}(x, y)$ is written as a function of its 2-dimensional Fourier spectrum, $\mathbf{A}(k_x, k_y)$, it can be shown that

$$\mathbf{E}(x, y, z) = \int_{-\infty}^{\infty} \int_{-\infty}^{\infty} \mathbf{E}(k_x, k_y) e^{i(k_x x + k_y y)} e^{iz\sqrt{k^2 - k_x^2 - k_y^2}} dk_x dk_y \tag{39}$$

is a solution to equation (38). Equation (39) can then be used to propagate a wave between 2 planes, such as a Gaussian wave at z=0 propagated to the z=z_0 plane. Firstly, the Fourier Transform of $\mathbf{E}(x, y, 0)$ is taken to gain the spectrum $\mathbf{A}(k_x, k_y, 0)$. This is then multiplied by the propagation kernel, before taking the IFT to recover the wave at the desired plane. Presented in a simple form, the angular spectrum algorithm is

$$\mathbf{E}(z_0) = \mathcal{F}^{-1} e^{iz\sqrt{k^2 - k_x^2 - k_y^2}} \mathcal{F}\mathbf{E}(0). \tag{40}$$

A result from the operation of this algorithm is illustrated in figure 10, where $z0$ is set as 2mm. Each point of the wave is plotted using MATLAB. The ASM is not only limited to

simple plane-to-plane propagation, masks can also be incorporated to generate diffraction patterns. Simulation of speckles and Talbot traps is then possible.

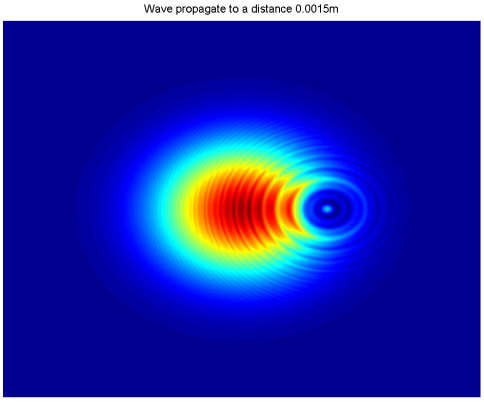

Figure 10: The result of simulating a Gaussian wave propagated to a distance of 0.0015m past a spot in the angular spectrum method, forming a speckle-like noise effect.

2.5.2 Validity of Angular Spectrum Method

Errors can arise when using the ASM. Consider the simulation in figure 11, very similar to the case of figure 10 but instead at a propagation distance of 0.004m. An interference-like pattern is then produced. This is caused by aliasing. Aliasing occurs due to an overlap of the signal in the spectral domain, resulting in loss of information.

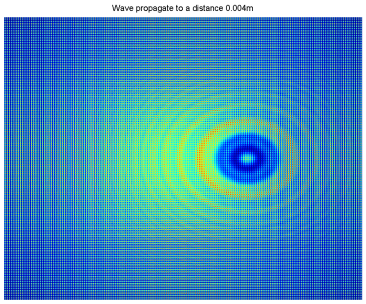

Figure 11: An example of the effects of aliasing for a propagation similar to figure 10.

Consider the diffracted wave in the ASM as a convolution of the form

$$\psi(x,y,z) = \mathcal{F}^{-1}\left[\mathcal{F}\left[\psi(x,y,0)\right] \times H(kx,ky,z)\right], \tag{41}$$

where

$$H(kx,ky,z) = \exp\left(iz\sqrt{k^2 - k_x^2 - k_y^2}\right). \tag{42}$$

In order to perform a successful IDFT, both $\mathcal{F}[\psi(x,y,0)]$ and $H(kx,ky,z)$ must be well sampled. For a two dimensional, symmetrical grid with M sampling points in the x-y plane, the central region of WxW pixels will be illuminated. Only the W pixels are then non-zero. For the simple case where $\psi(x,y,0)$ contains only 2 signals, the maximum propagation distance achieved without aliasing is given by [27]

$$z \leq (M-W)\sqrt{\Delta_x^2 - \lambda^2}\frac{\Delta_x}{2\lambda}. \tag{43}$$

Sampling separation can then be increased to allow larger propagation distances, although the object spectrum would need to be shortened. Alternatively, zero-padding can be performed whereby the pixel number(M) is increased while retaining the object size (W).

2.5.3 Gerchberg-Saxton algorithm

The GS algorithm is a common phase retrieval technique that works through Fourier transformations between diffraction planes, with the application of measured data or known constraints[28]. Relevant operations in this algorithm are illustrated in figure 12.

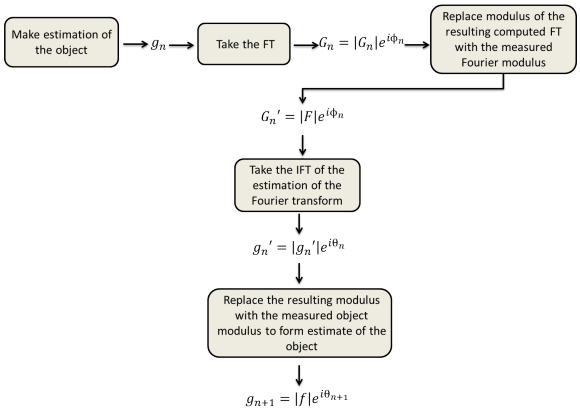

Figure 12: Flowchart outlining the steps in the GS algorithm.

The algorithm follows 5 general steps:

1. Make an estimate of the object.
2. Take the Fourier transform.
3. Replace the modulus of the computed Fourier transform with the measured Fourier modulus. This gives an estimate of the Fourier transform.
4. Take the IFT of the estimation of the FT.
5. Finally, replace the modulus of the resulting computed image with the measured object modulus to form a new estimate of the object.

Mathematically, for the nth iteration of this process, the algorithm can be represented by

$$G_n(k) = |G_n(k)|e^{i\phi_n(k)} = \mathcal{F}[g_n(x)] \tag{44}$$

$$G'_n(k) = |F_{meas}(k)|e^{i\phi_n(k)} \tag{45}$$

$$g'_n(x) = |g'_n(x)|e^{i\theta'_n(x)} = \mathcal{F}^{-1}[G'_n(k)] \tag{46}$$

$$g_{n+1}(x) = |f(x)|e^{i\theta_{n+1}(x)} = |f(x)|e^{i\theta'_n(x)}. \tag{47}$$

2.5.4 Error-reduction algorithm

Improving the accuracy of the GS algorithm, a generalized form can be implemented to reduce the error on each iteration. Regarded as the error-reduction generalization of the GS algorithm, a set of constraints in the object and Fourier domains are introduced. When transforming between planes, these constraints are satisfied before moving to the next step. For example, the object domain constraint may be applied in the form

$$g_{n+1}(x) = \begin{cases} g'_n & \text{if} \quad x \in \gamma \\ 0 & \text{if} \quad x \notin \gamma \end{cases} \tag{48}$$

for γ being the set of points that violate the object domain constraints. Included in this may be where the object estimation is negative, or exceeds the known object diameter calculated from the autocorrelation function[28]

$$f_{AC} = \mathcal{F}^{-1}[|F(k)|^2]. \tag{49}$$

Iterations of the algorithm continue until both the object and Fourier domain constraints are satisfied, allowing measurements on multiple diffraction planes and a reduction of error in phase retrieval.

2.5.5 Reduction of error in GS algorithm

Squared error in the Fourier domain is defined as the sum of the squares of the amounts by which the computed FT violates the Fourier domain constraints. In the Fourier domain, this error is [28]

$$E^2_{F,n} = \frac{1}{N^2}[G_n(k)| - |F(k)|]^2, \tag{50}$$

and for the object domain

$$E^2_{o,n} = [g_{n+1}(x) - g'_n(x)]^2. \tag{51}$$

A solution has been identified when these errors are zero. Recalling Parseval's theorem,

$$|f(x)|^2 dx = |F(k)|^2 dk, \tag{52}$$

equation (50) is expressed as

$$E^2_{F,n} = [g_n(x) - g'_n(x)]^2. \tag{53}$$

$g_n(x)$ and $g_{n+1}(x)$ both satisfy the object domain constraints, because $g_n(x)$ is an estimation of the object, based on the object constraints. and $g_{n+1}(x)$ is formed from the minimum changes made in $g'_n(x)$ to satisfy these constraints. Additionally, for all x, $g_{n+1}(x)$ is the closest value to $g'_n(x)$ satisfying these constraints. Therefore, $|g_{n+1}(x)| \leq g_n(x)$. Using equations (50) and (51) it can be shown that

$$E^2_{o,n} \leq E^2_{F,n}. \tag{54}$$

Error in the object domain is then always less than, or equal to, the associated error in the Fourier domain. Parsevals theorem can again be used, in the object domain, so that

$$E^2_{o,n} = \frac{1}{N^2}[G_{n+1}(k) - G'_n(k)]^2. \tag{55}$$

Similar to previous considerations, $G'_n(k)$ and $G'_{n+1}(k)$ satisfy the Fourier domain constraints. $G'_n(k)$ is the closest value to $G'_n(k)$ that satisfy these constraints at all k and, using equations (54) and (55), it is possible to show that

$$E^2_{F,n+1} \leq E^2_{o,n} \leq E^2_{F,n}. \tag{56}$$

Repeated iterations then result in an error that decreases or stays the same.

3 Methods

3.1 LASER and optics design and construction

In order to gain a reliable source of imaging light for holographic microscopy, a particular system was required. Figure 13 depicts the general set-up used in this experiment. Details, and basic operation, of the laser source and optical components will be described here.

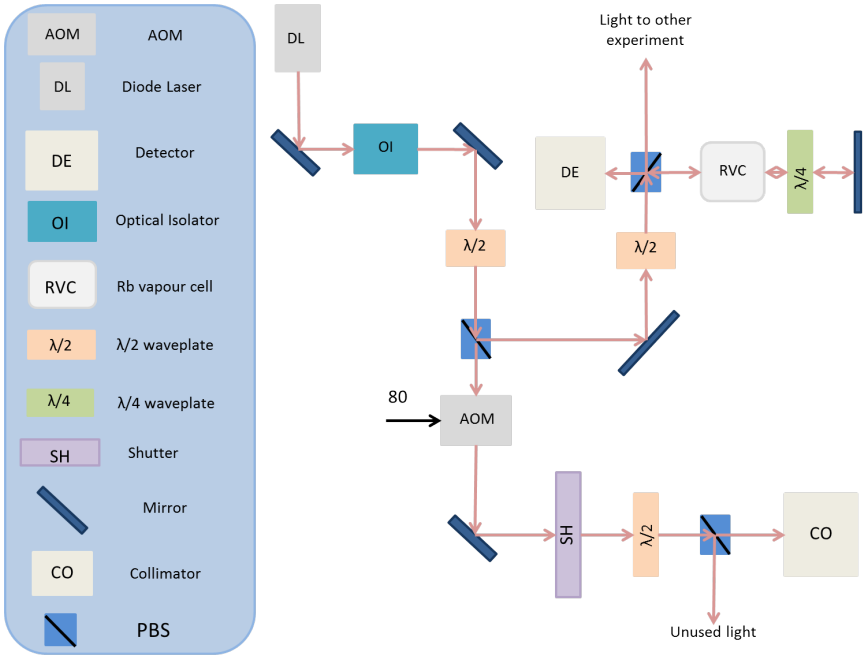

Figure 13: A schematic depicting the optics used in this experiment. The Acousto-optical modulator (AOM) has an $80H_z$ frequency input whose voltage input may be controlled between 1 and 0 volts to alter the intensity of the 1^{st} order beam. The unused light from beam splitters are used by other experiments in the same lab.

3.1.1 LASER system

A Uni Quanta ECL801 diode laser was used, and controlled with an ECL801-D controller. Using the system described in figure 13, the laser was initially locked to the atomic transition of Rb in the vapour cell. Location of the resonance peak was performed with the PZT controller to adjust the signal on the oscilloscope. Locking was tested by observing the error response to induced vibrations in the system. With an appropriate response, locking ensured that the laser source had a narrow bandwidth. During measurements the laser was allowed to scan by around 1 GH_z, implemented to reduce etaloning noise from the CCD.

3.1.2 Optics system

Minimizing optical feedback into the diode laser, an optical isolator was placed immediately after the mirror. Output from this isolator was directed through a $\lambda/2$ waveplate, and polarization beam splitter (PBS). The purpose of this was to control the amount of light transmitted to the rest of the system by altering the polarization with the waveplate. Adjustments changed the proportions of reflectance and transmittance through the PBS. Splitting of the light was used as a means of dither locking the diode laser to the atomic resonance of Rb.

In one path of the beam, light was again reflected by a mirror through another $\lambda/2$ waveplate, PBS pair. Some light was then transmitted through a Rb vacuum cell, $\lambda/4$ waveplate

and mirror. This was then reflected back on itself to the detector, connected to an oscilloscope. Adjusting the $\lambda/4$ waveplate then changed the proportion of light that is transmitted. Light entering the detector was used for dither locking the laser, important for holographic microscopy. Phase retrieval with the GS algorithm assumes only distance changes. Variations in the wavelength can then reduce the fidelity of phase retrieval (although extremely small changes should only appear as small amounts of noise in final phase retrieval, not completely tarnishing the fidelity of image reconstruction).

For the second path, light passed through an acoustic-optical modulator (AOM). A description of how this device works can be seen in appendix A.0.2. Output from the AOM was reflected by a mirror, through an open shutter and $\lambda/2$ waveplate, PBS pair, before being collected by the collimator. Light was then transferred to an optical fibre, the output of which was used in the imaging system. Only the first order beam from the AOM was collected, allowing precise control of the imaging laser frequency. Alignment was performed using an oscilloscope, connected to the fibre output, and finely adjusted until the signal was maximized. This ensured maximum transfer efficiency between the collimator and fibre output (preferably 50 percent in most applications).

Using the arrangement in figure 13 ensured a stable laser source that could be used for holographic microscopy with the set-up in figure 14. After collimation of light from the fiber output, it was then passed through an objective with an NA of 0.4 (only about 0.3 was actually used due to the size difference between the collimator output and objective input). This component focussed the collimated light. Both the hemisphere lens and pattern plate were mounted separately, allowing focussing on the entire pattern or different sub-patterns on the plate. Interactions between the pattern and this light then generated the scattered wave front that co-propagated with the probe beam.

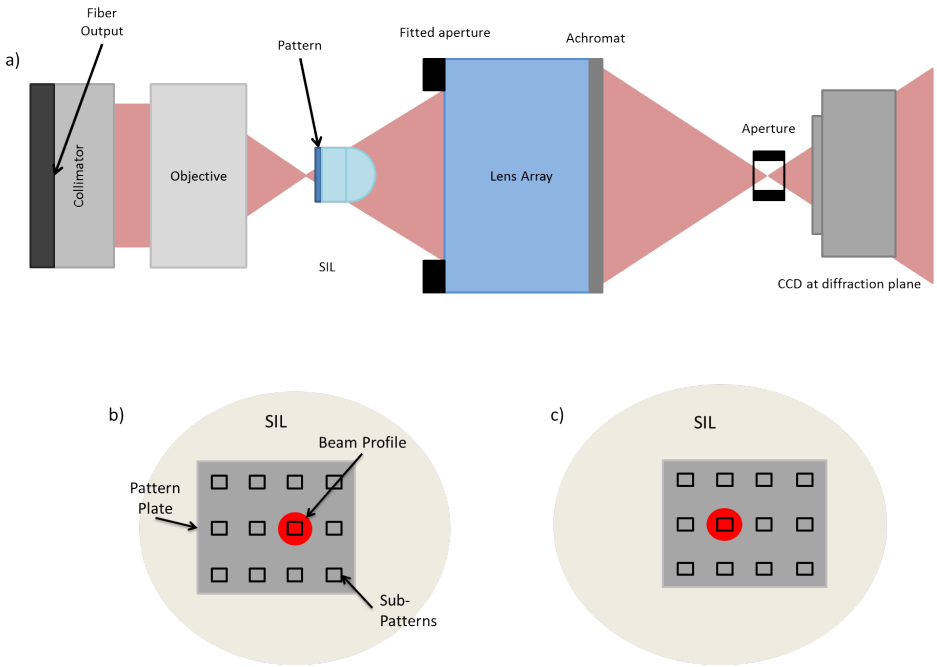

Figure 14: (**a**)Schematic diagram of the optics system after the fiber output. The red shade shows the beam motion through the system. (**b**) shows the beam profile highlighting a pattern on the plate, with (**c**) then showing the plate translated so that the adjacent pattern is illuminated. It is also important to note that the beam profile is positioned to the centre of the hemisphere. For details on the Solid Immersion Lens setup, see the appendix section, A.0.2.

Both wavefronts were captured by the lens array, with a fixed aperture attached to cut out diffusive light. Adjustment of the individual lens positions allowed collimation of the light. Additional benefits of this component were to increase the NA of the system and allow correction of aberrations. After passing through the lens array, light was focused by an achromat that allowed two different wavelengths of light to be focused to the same position, reducing chromatic aberrations. Figure 15 illustrates the passage of light through the hemisphere lens and lens array.

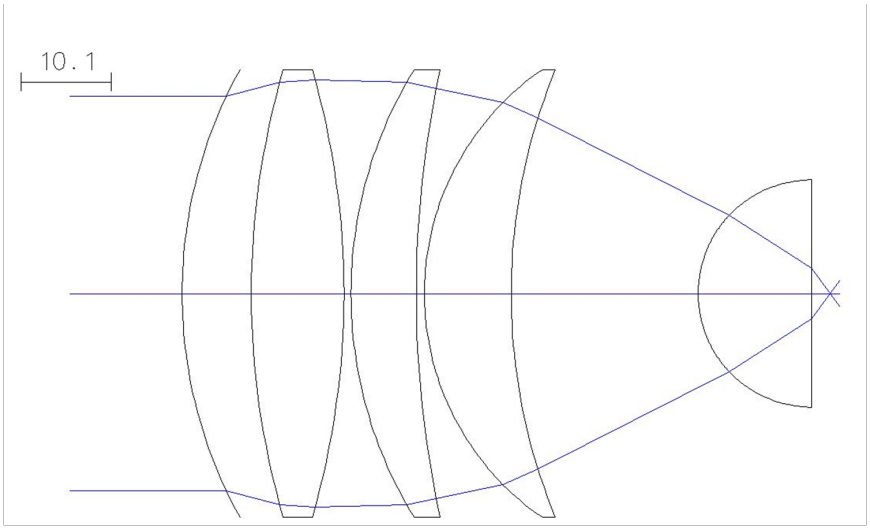

Figure 15: Schematic diagram of the lens array, including solid immersion apparatus, including a scale and ray diagram. Note that this excludes the achromat and the patterned plate.

Translating the CCD to multiple diffraction planes, images were taken and used for image reconstruction. This CCD chip was surrounded by a glass plate, potentially giving rise to etaloning noise. An additional aperture was included at the image plane to partially correct for this, where adjustments could be made to only encapsulate the beam profile. Reflections were then reduced. Removing all but the beam profile also ensured information from the probe and scattered light were not lost.

To minimize noise from vibrations/motion, the laser and optics systems were placed on an isolation system. Noise from lighting was minimized by blocking all paths for external light onto the imaging system. Uisng coaxial cables and twisted pairs, where necessary, ensured cross-talking was not a major source of error due to other equipment's cables. Addition of a climate control unit also minimised thermal fluctuations.

3.1.3 Automated system

The system incorporating figures 13 and 14 was almost entirely automated. Operation was then made much simpler, and more accurate, when translating the camera to further diffraction planes. Automation was initialized and controlled with Cicero using the operation procedure outlined in figure 16.

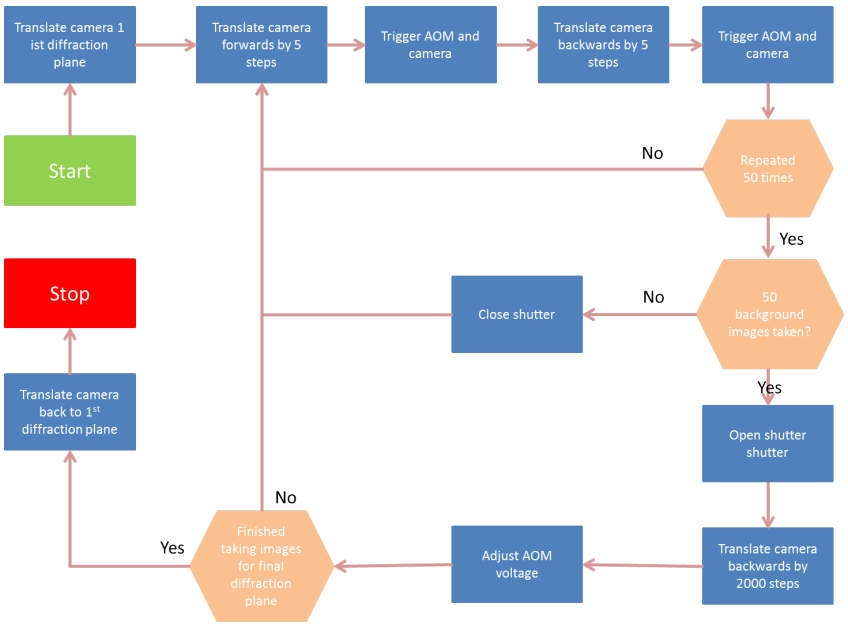

Figure 16: The flowchart for the automated image collection using Cicero.

Triggering of the camera to take images was applied in Cicero. Additionally, to reduce distortions from etaloning, the sequence in Cicero was modified to shift the camera forwards and backwards from the diffraction plane by 5 steps (each step being approximately 0.625μm). Images were then taken at these positions. Fifty repetitions were carried out so that a total of a hundred images were recorded. For background images, the signal to the shutter was removed, causing it to close. This sequence then repeated the same imaging procedure for a further fifty repetitions so that a total of a hundred plane and background images were stored for each diffraction plane. Camera translation was then triggered to move away from the previous plane by 2000 steps. An important point here, however, is that moving the camera away from the source reduced the counts recorded by the CCD. It was desirable to maintain relatively high count rates across all the planes (consider section 2.4.4), achieved by going through each plane individually, before the experiment, recording the AOM voltages required to maintain count rates of approximately 40000 out of a maximum of 65552. Voltages were imported to a list in Cicero, automatically adjusting the AOM voltage at each translation stage of the camera. After doing this, the procedure of shaking the camera and taking plane and background images was carried out. Translation of the CCD to the next diffraction plane was triggered, repeating the imaging procedure. This process was then repeated for a specified list of planes. At the final diffraction plane the camera was triggered to return to the initial image plane, meaning further experiments could be carried out without need for adjustments.

While the imaging sequence was fully automated, the source images were not. Referring to section 2.5.3, estimations of the source at the initial plane of the GS algorithm were required. Images at the source focal point, propagated to the final diffraction plane, were used as this estimation. Moving the camera in front of the image plane until only a small spot, corresponding to the source focus, was observed, images and background were recorded. Moving the camera forward, however, increased the counts on the CCD. Voltage to the AOM then had to be set to its minimum, and the $\lambda/2$ wave plate adjusted, to achieve the desirable count rate.

Keeping this waveplate orientation, however, produced a count rate of only a few thousand at the furthest diffraction plane. Even with the maximum AOM voltage this was apparent. Images of the source were then first carried out, before adjusting the waveplate to facilitate an appropriate count rate for the most distant plane. Ideally, everything would have been automated such that no changes had to be made, but this was not a very cumbersome task and didn't affect the overall quality of results. After taking the desired images, the pattern plate was translated slightly with the same imaging procedure being implemented. Sets of images were then recorded for these two positions.

3.2 Pattern fabrication

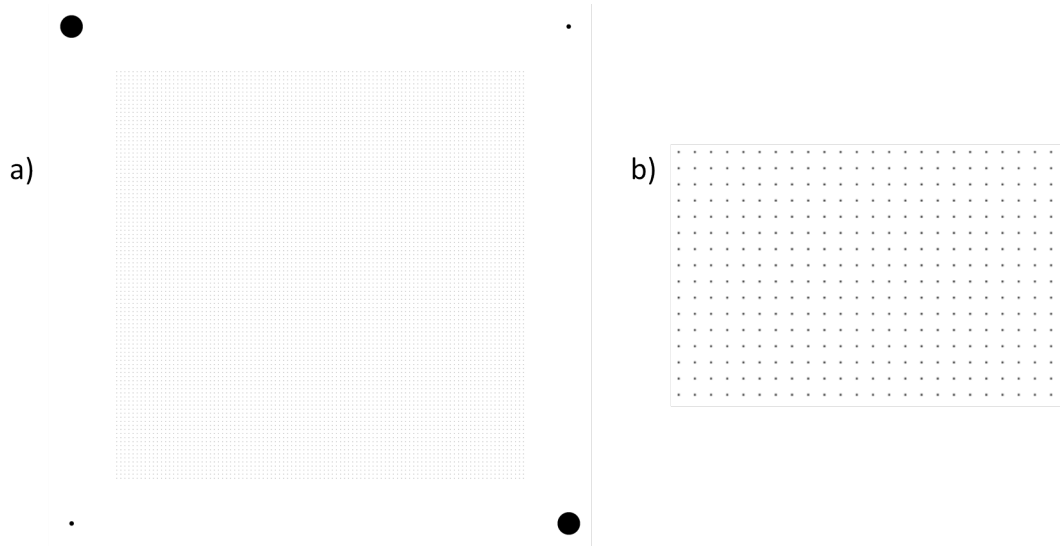

Figure 17: Example of one of the many patterns fabricated on the plate. (**a**) illustrates a particular example of a square array, with disk size and period of 0.1μm and 1μm respectively, while (**b**) shows a zoomed in image of the pattern. Also shown are the 1μm and 5μm disks fabricated at the corners of all the individual patterns.

For a variety of patterns, already outlined in section 2.2, holographic microscopy was performed using a single plate composing these varying patterns, but with different parameters. Electron beam lithography (EBL) was implemented for fabrication. For a 10x10 grid, square, hexagonal and Penrose patterns were fabricated with varying disk sizes and lattice periods. Each spanning a region of 10x10μm^2, an additional 10μm around each pattern was introduced. Within these regions, 1 μm and 5μm disks were fabricated to allow optimisations with Zernike functions. MATLAB was used initially to create these patterns, with the code illustrated in appendix ..., before fabrication. An example of such a pattern is shown in figure 17.

3.3 Algorithms for image retrieval and simulation

3.3.1 Image reconstruction

Image reconstruction with holographic microscopy, using the system outlined in figures 13 and 14, was performed with images taken at various diffraction planes, taken with the process described in section 3.1.3. Diffraction plane images were manipulated with the code presented in appendix A.0.3. This code follows the ERGS algorithm detailed in section 2.5.4. A few general remarks on this code can be made. A Gaussian wave propagated to the final diffraction plane was used to provide the initial phase, and the measured distribution at the plane used as the magnitude. After propagation of this distribution to the first plane first, the measured distribution at this plane was compared with the estimation, from the propagated Gaussian wave, using the logical matrix *kwindow* as the spatial filter for the Fourier domain constraints. This filter was formed from the maximum possible spatial component of the wave. Optimizations of this distribution were then performed with *fminunc* to minimise the difference. Three planes were chosen so as to encompass the entire movement of the camera when taking images, Iterations between these planes continued for a specified number in order to improve the fidelity of the phase retrieval, recovered from the final, calculated field distribution. Residue between the absolute square of the measured and calculated distributions was monitored to observe the change in the error as a function of iteration number.

After carrying out the ERGS algorithm with the two sets of images, the reconstructed diffraction plane images were propagated to the focal plane. The difference between the two images was then taken. Optimizations, made to the amplitude of one of the distributions, minimized this difference. Aiming to remove the background noise that should have been the roughly the same in both images, these optimizations also meant that the spots of the translated image appeared as intensity minimum. Only the first image points were then observable. To correct for aberrations, Zernike functions were additionally implemented. Application of these functions were performed by isolating a particular region of interest on the image. For this experiment, the disks at the corner of the patterns were chosen. Aberration coefficients were minimized with application of the Zernike functions to these isolated objects. Firstly, the distribution was multiplied by a matrix, cutting everything out except the region of interest, and the reference removed. After squaring the subtraction, each Zernike function was summed. Minimisation was again performed to retrieve the function minimum, each of which corresponded to a type of aberration. In the ideal case this would be reduced to zero such that no aberrations exist but, failing to achieve this, best improvements were made until the subtraction region appeared most focussed. Different orders of the functions were tested until this was achieved. Corresponding corrections were then applied to the entire image to reduce the overall effect of aberrations and improve the overall image quality. Code devloped to perform these corrections can be studied in appendix A.0.5.

3.3.2 Angular spectrum method: Pattern and Trapping Simulations

As discussed in section 2.2, this thesis aims to explore the revival effect in quasi periodic patterns. Here, the Talbot and Montgomery effects are simulated for a variety of patterns. In

general, the masks have been modelled as a series of disk-shaped holes to allow the transmission of light. For the Penrose pattern, this was extended to a series of disk-like scatters to block the light. Light with normal incidence, and at 45 degrees, to the pattern have also been simulated to compare effects on the Talbot length and intensity.

To compare regions of self-imaging with predicted Talbot lengths, expressions defined in section 2.2 have been used. For the square and hexagonal array in the para-axial limit, this is very simple. Expressions (9) and (14) can simply be calculated from the light and lattice parameters. Beyond this para-axial limit , approximations have instead been made. In expressions (11) and (15), $n^2 + m^2$ has been chosen to be equal to 1 so that

$$Z_{R,Sq} = \frac{\lambda}{1 - \sqrt{1 - \left(\frac{\lambda}{a}\right)^2}}, \tag{57}$$

and

$$Z_{R,Hex} = \frac{\lambda}{1 - \sqrt{1 - \frac{4}{3}\left(\frac{\lambda}{a}\right)^2}}.. \tag{58}$$

For the square, this is equivalent to defining $\frac{a}{\lambda}$ in the range $1 \leq \frac{a}{\lambda} < \sqrt{2}$. From figure 4, only plane waves with $n^2 + m^2 = 1$ need be considered. Perfect self-images can then still possible. For the hexagon, this assumption is less valid as the indices are not as neatly defined.

Code developed to simulate the Talbot and Montgomery effects can be studied in appendix A.0.5, following the algorithm described in section 2.5.1. Simple functions have been created to simulate the square and hexagonal array. Penrose pattern simulation follows the algorithm described in [19]. An additional factor N can be changed to adjust the lattice period of the patterns, in addition to allowing the choice of holes or disk like scatterers. Diffraction effects resulting from these patterns can also be simulated for any angle of incidence, over a set region of space and step size, for different types of atoms and atomic resonance lines. Trapping depth and scattering rate are then determined from (5) and (4). To avoid possible effects of aliasing, arising as a result of using the Fast Fourier Transform (FFT), saved images were zero-padded, Validity of the simulations was then ensured, for the reasons discussed in section 43.

4 Results

4.1 Holographic image reconstruction

Two sets of images were taken for each particular pattern of interest, the difference being a slight translation of the pattern with respect to the hemisphere. Only images of key planes, at different stages (reconstruction and pre-reconstruction), are placed in this section due to the large number of planes recorded.

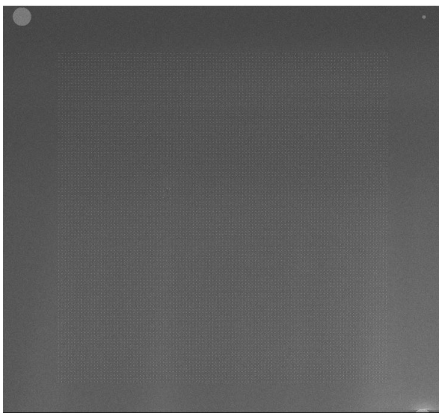

Figure 18: An SEM image taken of an exemplar pattern, created on MATLAB such as in figure 17, produced by e-beam lithography

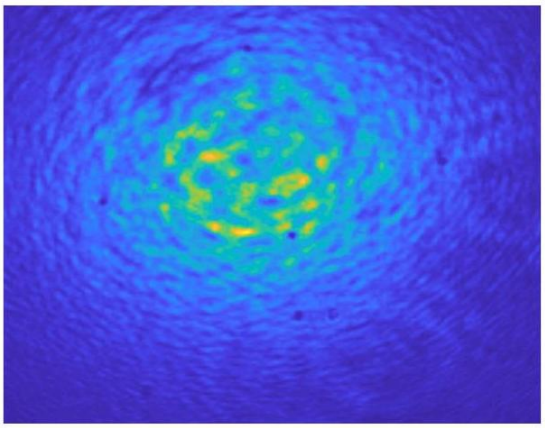

Figure 19: A raw image taken with the CCD at the focal plane of the pattern. The image is zoomed in onto a selection of the wavefront for closer inspection of the 5 micron spots.

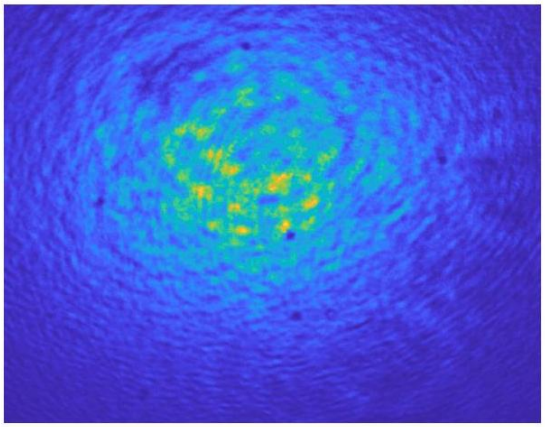

Figure 20: Reconstruction of the focal plane of the pattern post phase retrieval. The image is zoomed in onto a selection of the wavefront for closer inspection of the 5 micron spots. To notice are the small differences in this image and figure 19,such as the presence of extra fringes and the apparent lack of focusing of the 5 microns spots.

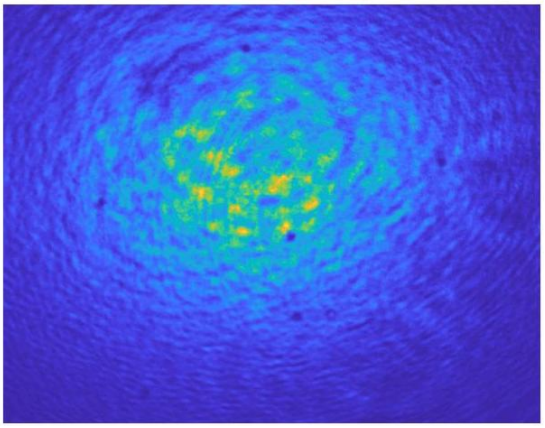

Figure 21: Reconstruction of the focal plane of the pattern, post-corrections, using the CCD image. The image is zoomed in onto a selection of the wavefront for closer inspection of the 5 micron spots. Although difficult to distinguish, the visible differences are the shifting in position of spots and fringes. Upon finer inspection, small changes to the spots can be seen on the individual pixel level.

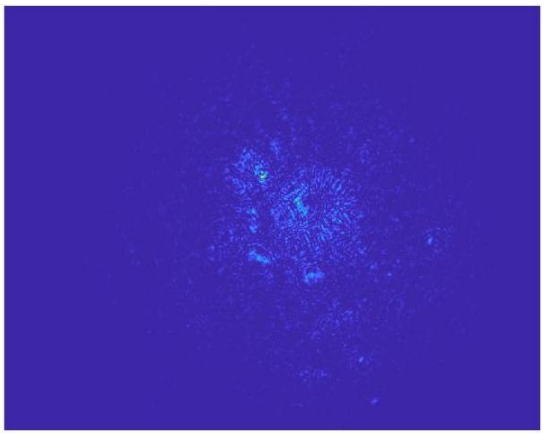

Figure 22: Reconstructed image of the differences between intensities at the focal plane, pre removal of noise.

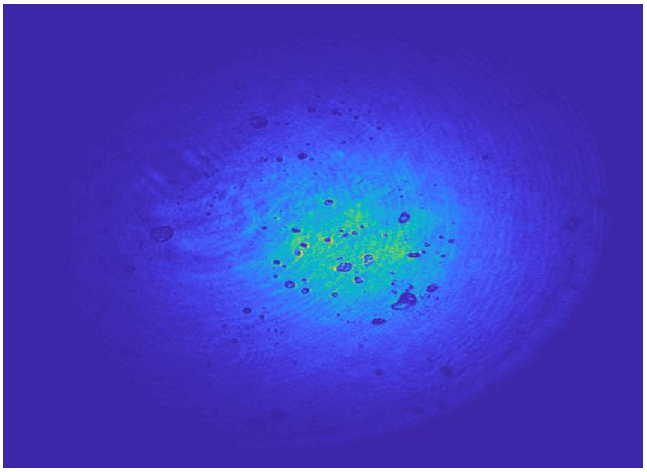

Figure 23: Image of a focal plane behind the pattern, possibly representing impurities or dust particles on the objective piece's lens.

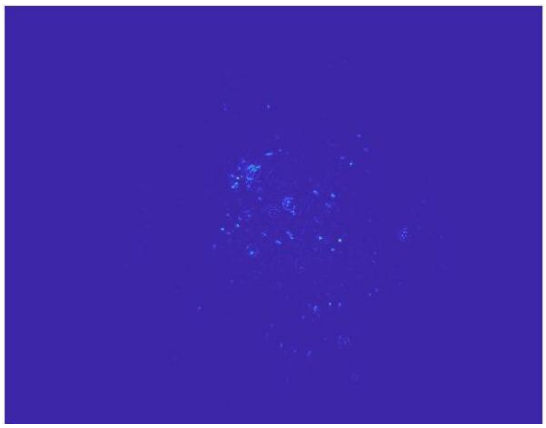

Figure 24: Reconstructed image of the differences between intensities at the focal plane, post removal of noise. It is clear that noise reduction has been successful, with the elimination of many of the fringes and a selection of other spots spanning the central region. The remaining bright spots are either the spots from fabrication or from impurities on the patterned surface.

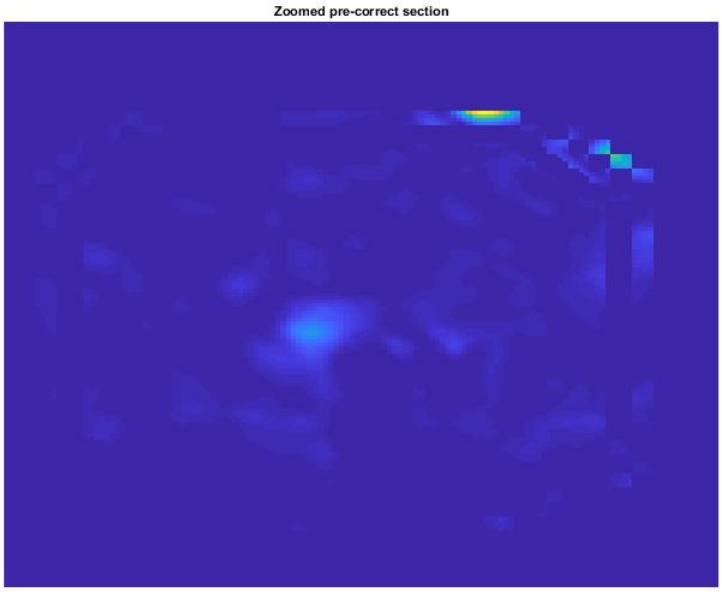

Figure 25: A magnification and isolation of one of the five micron spots on the image in figure 24. This spot was selected to apply aberration corrections.

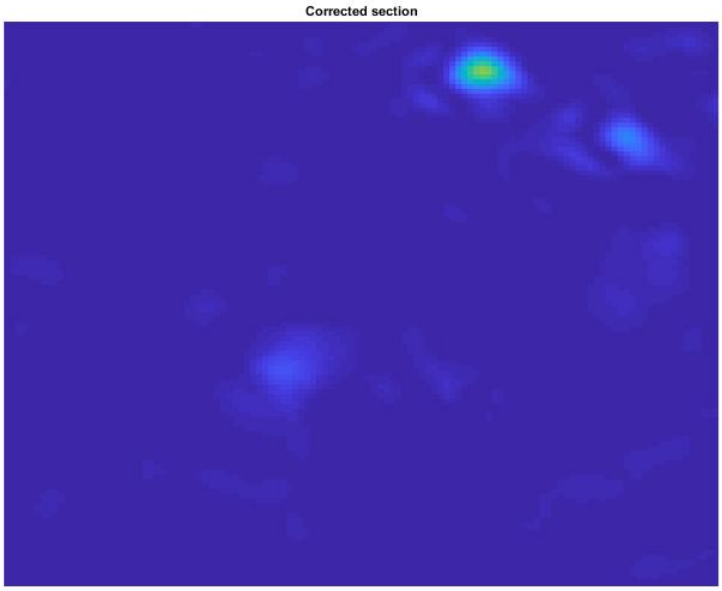

Figure 26: Reconstructed image of the differences between intensities at the focal plane, post attempt at removal of aberrations. The one difference to notice is an adjustment of intensity (seen by the change in colour), and the minor shape change.

4.2 Talbot trapping simulation results

4.2.1 Square Array

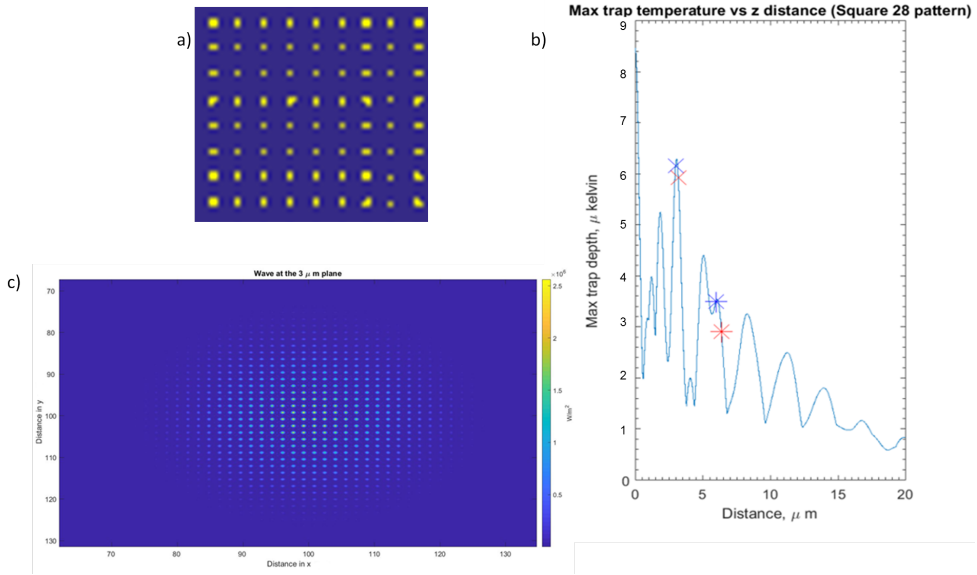

Figure 27: Simulation of the ASM for wave propagation through a square array mask with $\frac{a}{\lambda}$ equal to 2. (**a**) represents a cross-section of the simulated pattern, while (**b**) illustrates the evolution of maximum trap depth with propagation distance. Red and blue crosses correspond to the Talbot length approximations in (9) and (57) respectively. (**c**) shows the intensity distribution at z=3μm. Propagation vector of the wave is normal to the surface, and the colourbar indicates the intensity corresponding to each point in the x-y grid. The grid axis are in units of pixels, each of which correspond to 0.05μm.

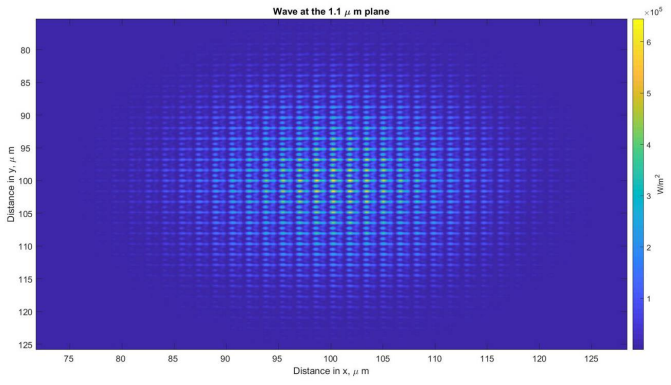

Figure 28: Simulation of the ASM for wave propagation through the same mask as in figure 27, but at 45 degrees to the surface. (**a**) illustrates the change in the evolution of the trap depth with the propagation distance, where the blue crosses are the Talbot length approximations of (57) multiplied by a factor of $\frac{1}{\cos(45)}$. (**b**) shows the intensity distribution at z=1.1μm.

4.2.2 Hexagonal Array

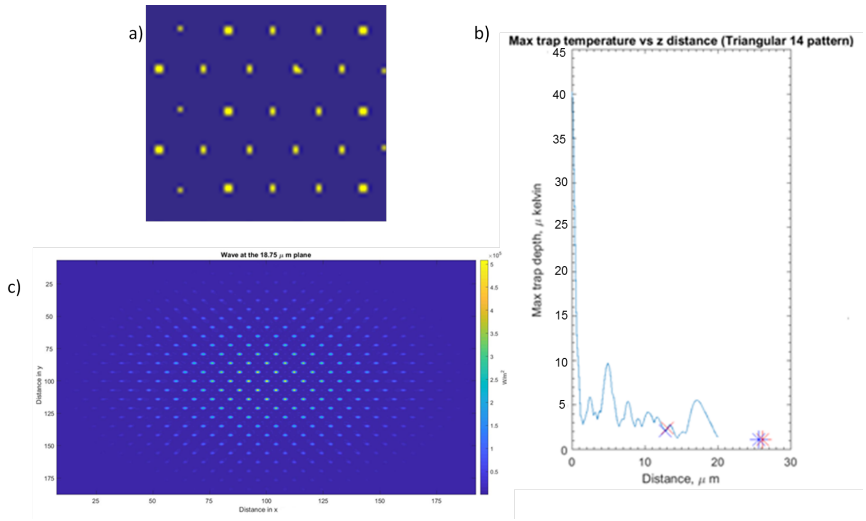

Figure 29: Simulated wave propagation through a hexagonal mask, with normal incidence, where $\frac{a}{\lambda}$ is approximately equal to 4. (**a**) illustrates a cross-section of this pattern. (**b**) represents the evolution of the maximum trap depth as a function of the propagation distance, where the red and blue crosses correspond to (14) and (58) respectively. For the z=18.75μm plane, the intensity distribution is shown in (**c**).

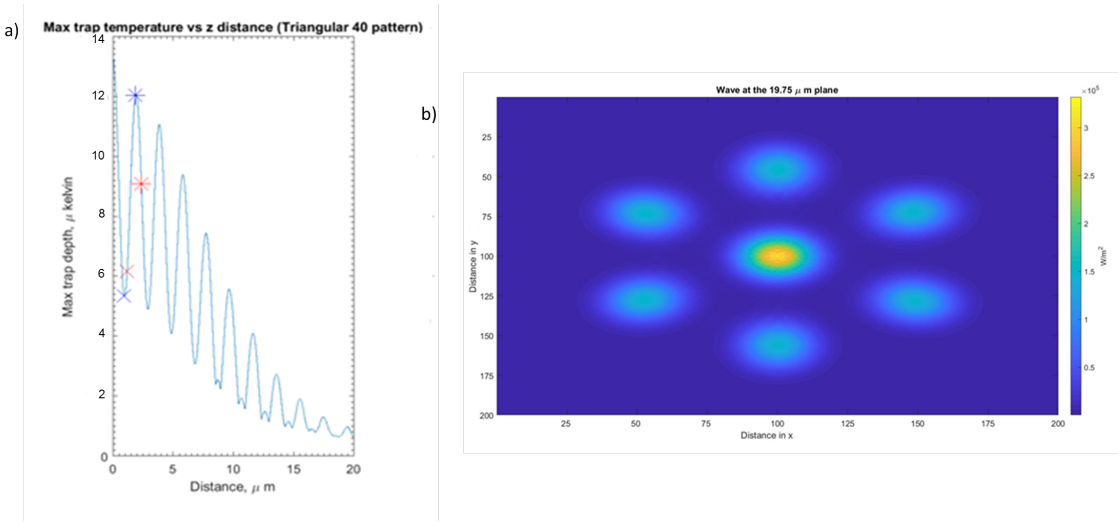

Figure 30: Simulation of wave propagation through a hexagonal mask with normal incidence. (**a**) illustrates the evolution of the maximum trap depth for a hexagonal array with $\frac{a}{\lambda} = 1.2$, with (**b**) representing the intensity distribution at the z=19.75μm plane.

4.2.3 Quasi-periodic array

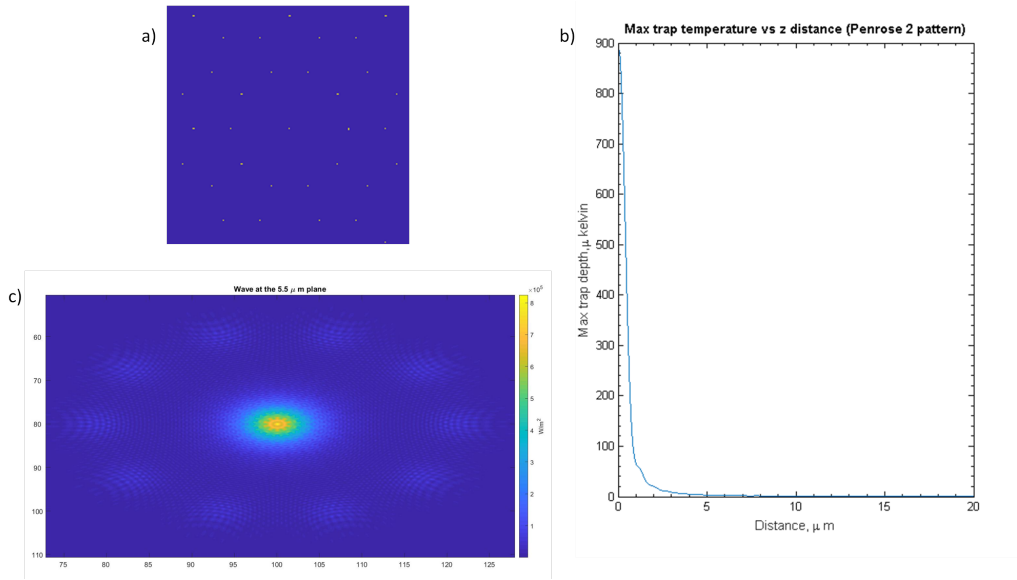

Figure 31: Diffraction effects resulting from a Penrose pattern with N=2. (**a**) shows the initial mask and (**b**) illustrates the maximum trap depth as a function of the propagation distance. (**c**) is an example of one of these planes, at z=5.5μm, and presents a possible location for atom trapping

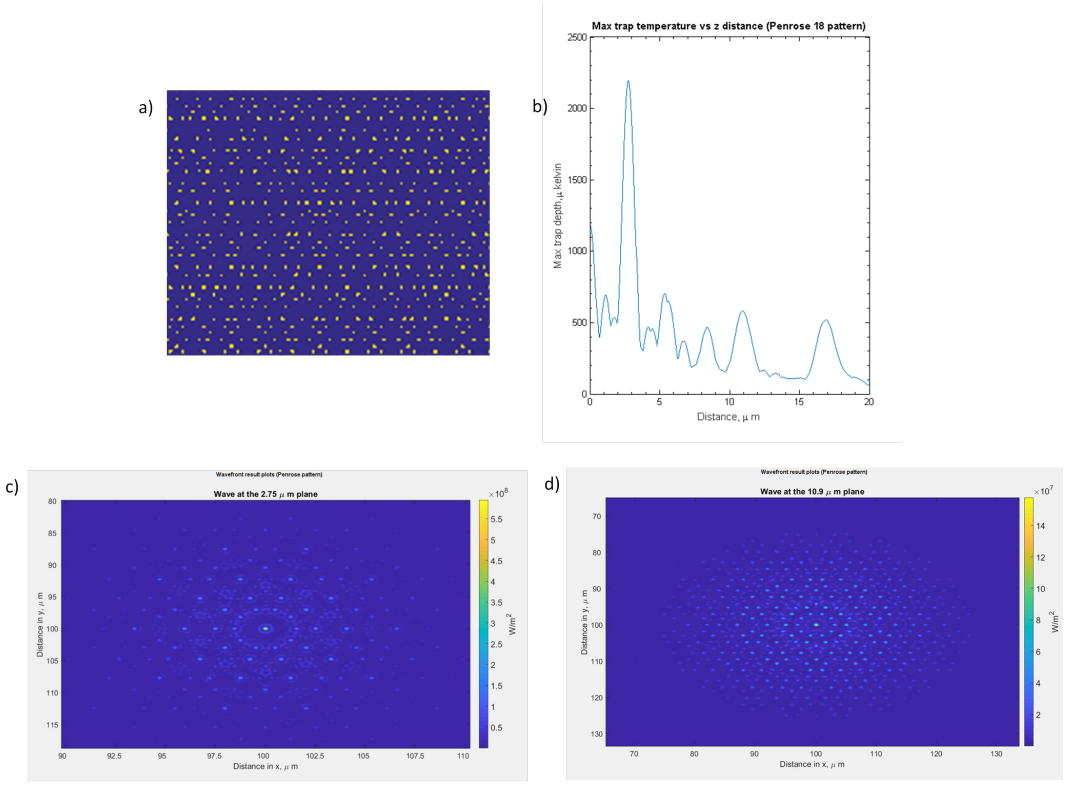

Figure 32: Diffraction effects resulting from a Penrose pattern with N=18, a much denser pattern than in figure 31. The initial mask can be seen in (**a**). (**b**) illustrates the change in the maximum trap depth with propagation distance. (**c**) and (**d**) are examples of planes at which trapping could be implemented, with differing potential landscapes

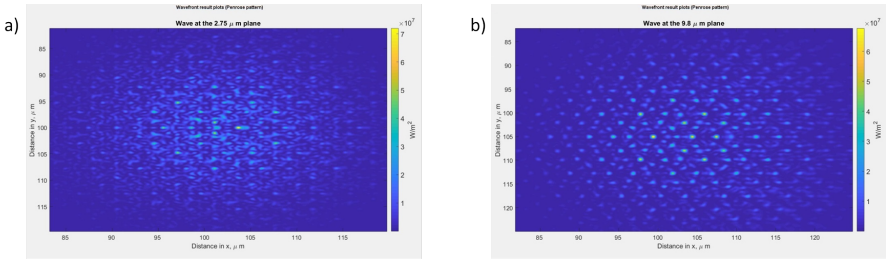

Figure 33: Illustration of Penrose scattering for N=18, at the same planes shown in figures 32(**c**) and (**d**), but with 45 degrees incidence.

5 Discussion and analysis of Results

5.1 Image reconstruction

Figure 18 illustrates an example pattern imaged in this thesis, and figures 19 and 20 are the images obtained from the CCD and the same plane reconstructed post-phase retrieval respectively. Without needing too close an inspection, clearly there are some differences, and

possibly the reconstructed image appears worse than the CCD image. Reconstructed images not only have errors from aberration, like the CCD image, but also the those introduced during phase retrieval with the GS algorithm. In the future this could be reduced by increasing the amount of planes that the GS algorithm iterates between. In the near future, however, this is difficult due to the increased requirement on computing power. Furthermore, readout noise from the CCD may not be removed via this method. One problem with this error is that the weaker signal from the smaller spots may not have been retrieved.

The GS algorithm's introduced error was removed by attempting to use the CCD obtained image to correlate the two images. Correction is mainly noticeable with lowest order Zernike functions as a shift defocusing correction(i.e. bringing the plane closer to the actual image focal plane). The correlation between the CCD image and the reconstructed image is improved by 0.001 (from 0.970 to 0.971), numerically indicating the minor improvement. Effects of the higher order terms are seemingly negligible, unless carefully inspected. Final corrected images still appear distinct to the raw image obtained directly by the CCD, meaning that the success in correcting for the error in the GS algorithm is minimal. Despite the minimal correction, it is still useful to proceed in even seeing the effect of aberration correction on a noisier image. The corrected image in figure 21 can be compared with figures 20 and 19.

Significant amounts of noise in this image possibly arise as a result of the large impurities on the objective, shown in figure 23. Focusing of these points with the ASM found them to be on the other side of the source plane, confirming their location. Attempts were made to remove the scatterers on this plane to reduce the effect on subsequent planes. In order to do this a subtraction was made between the two intensity planes, as explained in section 3.3.1. This was then propagated to the focal plane of these scatterers. Inversion of the image such that the dark spots became bright then allowed these impurities to be removed, the resulting image at the focal plane is shown in figure 22. Once the noise sources have been removed and then the corrected image re-propagated to the image focal plane, the Zernike functions can be applied to correct for aberrations around selected 5 micron spots.

The noise corrected image is shown in figure 24, where the bright regions correspond to some of the fabricated spots. Performing some of these corrections, as shown in figure 26 on a selected spot area in figure 25, it is possible to see there are some minor improvements around particular points of interest. Zernike functions, however, seem to have limited to near no effect and it is difficult to tell whether other spots on the image actually represent the smaller markers. It is also very difficult to make out any obvious presence of the smaller pattern of interest, possibly again due to the limited effect of the Zernike functions. Loss of some of the information due to these scatterers during phase retrieval could also be a significant factor in this.

There was a slight cut in the raw images provided to the GS algorithm. From reconstruction, this did not seem to have a huge impact, but still may have contributed to error in the phase retrieval. Initially, it was believed this cut was due to the final aperture. Returning to the experimental set-up, and checking the image without the aperture, it was found this cut was still present. The aperture could then not be the cause. Following the beam path, a number of other possible cutting points were identified. Firstly, the fixed aperture on the lens array. If slightly too large then light will be blocked. The second possible cause is the objective, as slight misalignment would result in cutting of a minor part of the beam. Finally, the hemisphere may

have also been misaligned, resulting in a similar effect.

5.2 Errors and noise in image retrieval

Multiple noises or errors could be classed as coming from, or controlled by, the environment. All of these will have affected certain parts of the experimental procedure. Typical in experiments, temperature may have been a cause for this. This can, however, be dismissed as a minor effect. The fibre, laser, camera and even the optics would have been affected by these fluctuations. For the fibre especially, when poorly coupled it would be more sensitive to a variety of noises. Even with implementation of the ERGS algorithm and Zernike functions, limited levels of noise can be effectively corrected for before the retrieval fails. For future experiments, the aim would be to replace the objective piece with a cleaner lens surfaces, decreasing the extent of required removal via the numerical techniques.

Initially, the patterns themselves generated a source of error due to fabrication with EBL. Errors then arose as inconsistencies between the disks, as shown in figure 34. Slants in patterns reduce the periodicity (figure **??**), making image capture and aberration corrections difficult. Several attempts at fabrication were then required to achieve a suitable group of patterns. Dust and other impurities on the pattern surface also resulted in focussed images of these distortions when propagating the image reconstruction. Unfortunately, unlike the imperfect objective, noise from the pattern surface could not be numerically removed as easily without risking the removal of the actual pattern points themselves. Information would then be lost.

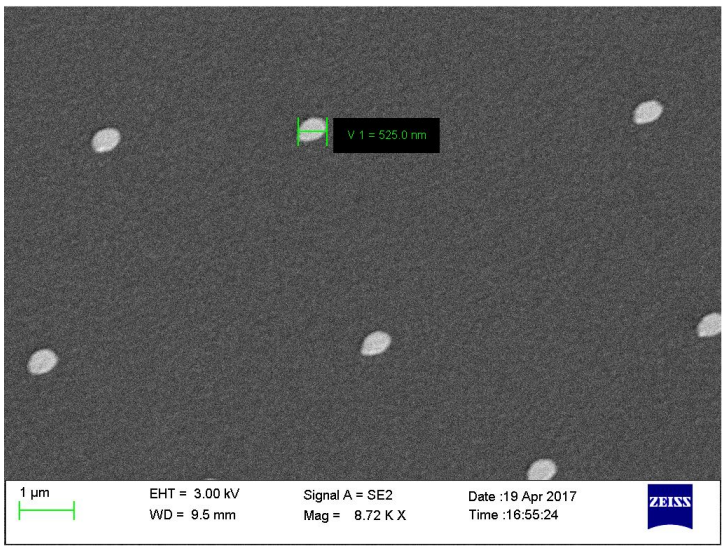

Figure 34: Scanning Electron Image (SEM) of a fabricated pattern, with diameter of a selected disk, to note are the small variations in shape and size between each disk.

Noises from room/desk lights, monitors, wiring and other light sources have been minimized as mentioned in section 3. External light could not be removed from the system entirely, but is far from the dominant source of error.

Spatially-coherent noise (SCN), an example of which is shown in figure 35, may be another source of noise. Fringes are best observed when the experiment in figure 14 has all of the lenses removed. The very thin substrate at the back of the CCD, glass cover or vacuum sealed window could cause etaloning. Noise such as this may reduce the ability to approach the shot-noise limit, possibly being a dominant noise source. One future modifications could be made to reduce some of these noises by randomizing the shaking of the CCD. Using Cicero, however, this is difficult to implement. Diffusive light mainly from the Hemisphere lens may also still be present, despite addition of the aperture on the lens array.

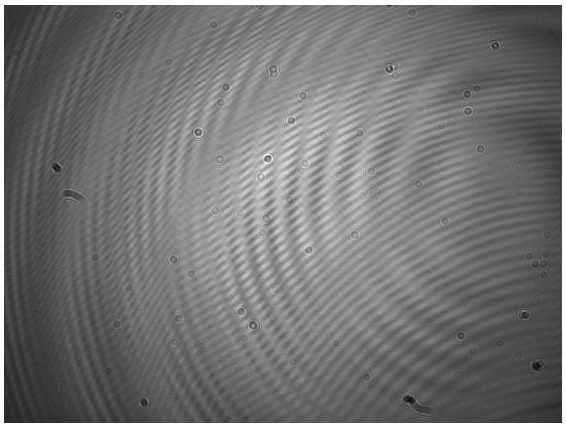

Figure 35: An image taken from a pco pixelfly CCD illuminated by a single mode laser. The large fringes are likely caused by CCD etaloning. The small spots are due to dust particles on the cover glass or collimator lens.

Noises from dust and other impurities, despite good cleaning of the lenses and application of aberration corrections, are still present. The lenses are not perfect either, with a scratch-dig (surface quality, with 0 being best) of 40-20. More noise is then introduced. Better performing scratch-dig lenses become much more costly, defeating the ambition of the experiment to create a simpler and cost effective method for cold atom imaging.

When performing dark count measurements without a shutter, and zero voltage into the AOM, some beam light coupling with the fibre was still observed. Some feint structure of the pattern was then being picked up by the CCD. Impurities in the AOM crystal likely caused this, resulting in natural Bragg reflection and so production of a very low intensity first order beam. The shutter then solves this problem. Background images were also averaged and subtracted from the main images. Main images themselves were then not affected by this as the only the intensity should have been changed. The voltage to the AOM was adjusted to manage this.

Alignment also affected the noise and error in the system. Figure 14 assumes ideal alignment between all optical components, but both ideal and non-ideal alignment can potentially contribute different noises. Ideal alignment could result in more etaloning (reflective) noises, the dominant noise. Slight misalignment means less reflective noise. Additionally, a tilted pattern plate is serendipitous as it provides an opportunity for testing the possibility of 3D imaging with holography. Other misalignments, such as the pattern not being in the middle of the sphere and a misaligned beam into the camera, contributed unwanted aberrations and inaccuracies into the image retrieval algorithms.

In addition to implementing and building upon the suggestions to tackle noises and errors in the system, further experimental procedural changes could also be made to improve results. By having the second set of images being taken as one of the 5 micron spots only, as opposed to the translation. Less noise would arise and corrections could be more easily applied. Corrected images could then be used as a first-stage correction plate to the full pattern images. There are additional ideas that can be used separately, or in combination. One of these includes using a patterned plate with a greater range of disk sizes, mainly adding sizes between 5 microns and 1 microns. Corrections could then be applied iteratively on spots reducing in smaller sizes. Cleaning of some of the surfaces to remove the speckle noise, reducing the need of greater numerical removal, would also reduce risk of information loss. Studying ways in which the loss of scattering from smaller scatters can be minimised experimentally, and through phase retrieval, would certainly make a difference when considering the smallest features. An optimal application of Zernike function corrections suitable for the research undertaken in this thesis also needs an expanded literature review.

As a whole, the attempt of this technique was too bold, starting off with too large a set of aberrations and noise to correct. Instead, it would be more ideal to develop the technique iteratively, tackling increases in noise and aberrations one by one. Many steps for this can be identified, including the ones mentioned above. Another step would be to simply attempt to correct a wavefront through the optics system without a pattern, and use this correction as another numerical correction plate. Another suggestion would be to improve the setup so that it more closely matches that of a hemisphere, which, at the moment is not the case.

5.3 Talbot simulations

5.3.1 Details regarding simulations

Before examining simulation results for the variety of patterns, some important points can be noted. Firstly, it is clear from the images that intensity peaks in the centre, simply due to the nature of the Gaussian beam simulated as the illuminating source. With this illumination, the beam is diverging. Images recovered at diffraction planes are then magnified copies of the original grating. Results also appear to have fringes towards the edge of the area occupied by the pattern, due to the finite nature of the pattern. Diffraction effects will then be less influential towards the edge where the fewer holes are present. Simulations have been carried out for propagation distances, with a maximum of 20μm. For greater distances than this, atom trapping is unlikely to be performed and so analysis of the Talbot and Montgomery effects in this regime has been ignored. Regrading the simulation parameters, the laser wavelength and power were chosen to be 780nm and 0.75W, with disk sizes and pattern widths set as 0.2μm and 200μm respectively. The beam was also simulated so that the beam waist coincided with the pattern, with a size equal to an eighth of the pattern size. Some simulations include the para-axial and non-para-axial Talbot length as crosses. The first points on these graphs correspond to half of these quantities, and so a phase shifted self-image, and the second set correspond to the perfect self-image distance.

For the Penrose pattern there is a fivefold symmetry. As discussed in section 2.2.3, partial revivals are expected when the Montgomery rings align with points in the reciprocal lattice.

Accurate prediction of the revivals then requires knowledge of various lattice periods. Due to difficulties in determining these quantities, the Penrose pattern revivals are simply observed and analysed. No quasi-Talbot length estimations are then presented in the Penrose simulations.

For an insight into the application of these traps to cold atoms, the trap depths and scattering rates have been calculated from (5) and (4). Additionally, trapping depth has been defined in units of temperature, using $T_{dip}(K) = \frac{2}{3k_B}U_{dip}$, giving a better insight into possible applications. General trapping analysis is undertaken using the D2 line of K39 and D1 line of Rb85 atoms, assuming the properties outlined in table 1. Both additionally used a laser wavelength of 780nm. The square and hexagonal arrays have been analysed with K39 atoms, while the Penrose pattern uses Rb85.

Atom	Wavelength (nm)	Saturation Intensity (Wm^{-2})	Spontaneous decay rate (ns^{-1})
Rb 85 (D1-line)	795	15.0	0.038
K 39 (D2-line)	767	17.5	0.027

Table 1: Relevant parameters used to determine the trapping capabilities for K39 and Rb85 atoms in the simulations

When discussing the applicability of these trap simulations to real world situations, there are further points to consider. Supporting the simulations presented here, finite disk sizes are assumed. This is a better, more realistic, simulation compared to many numerical investigations into the Talbot effect that use unrealistic point sources. Diffraction from the pattern changes between these assumptions. Having been defined in MATLAB, however, these holes are not entirely uniform and so the simulations are not perfect.

Propagation between planes has been performed using the ASM. It should be noted that inaccuracies are likely due to the scalar wave approximation of this method. Surface plasmon resonance resonance have also been ignored. Simulations in this thesis assume the wave is completely blocked by the areas of the mask where disks/holes are/aren't present. Realistically, however, this is not the case. Transmission through the pattern due to this resonance can occur, affecting the wave distribution at the diffraction planes. Having an incident wave at 45 degrees can result in total internal reflection, thereby reducing this effect. Simulations presented in this work then are still, at best, an approximation. Nevertheless, they allow a relatively detailed analysis of the Talbot/Montgomery effect and its particular applications for cold atom trapping.

5.3.2 Square array

Simulation of the diffraction effects generated by a simple square array can be seen in figure 27. (**a**) shows the initial mask, and (**b**) plots the evolution of the maximum trap depth as a function of the propagation distance. Z_T and Z_R are detailed on this plot, calculated from equations (9) and (57) respectively. Clearly the para-axial approximation is always greater than Z_R, corresponding to the Taylor expansion as the upper-limit. From (**b**), the para-axial Talbot length is obviously not very suitable as it does not coincide with the peaks in the trap depth.

This is due to the ratio of a and λ, in this case equal to 2, where the para-axial limit is not held. The blue crosses, however, are a much better match. Even this is not perfect, however, due to $\frac{a}{\lambda}$ being greater than $\sqrt{2}$, so the approximation in (57) is invalid. (**c**) represents the first revival of the pattern at 3μm. A phase shifted copy of the original grating pattern is then observed at this plane (see section 2.2.1). Structurally the image is a clear copy of the diffraction grating, albeit magnified due to the nature of the beam. Examining the capabilities for trapping atoms, the maximum intensity corresponds to a trap depth and scattering rate of approximately 6.12μK and 0.22Hz respectively, illustrating a slight possibility for atom trapping with the square array.

Figure 28 is a fractional Talbot plane where the light is incident on the same pattern, but at 45 degrees. Some structure is still visible, but definition is much lower than in figure 27. From the ideas developed in section 2.2.1, this is an expected result. Multiple copies of the pattern are superimposed at this plane, meaning the pattern becomes smeared out. A drag effect is also apparent, extending from each of the points. An explanation of this lies in the propagation direction of the wave. For propagation at 45 degrees to the pattern, following the wave with the ASM means the points will be shifted. Because the wave had a y-component equal to zero in these simulations, the shift occurs only in the x direction as opposed to moving diagonally.

Reasoning behind why this fractional plane is not extremely clear may come from $\frac{a}{\lambda}$ used for this particular simulation. The opening fraction of a pattern is defined as the ration of the hole diameter, d, to the lattice period such that $f = \frac{d}{a}$. If f is not sufficiently small then there will be a large overlap of the fractional plane images. Fractional planes then become less defined. Problems with this simulation may then arise as a result of the lattice period being too small. Incident light at 45 degrees to the pattern also means a break down of the para-limit. As discussed previously, perfect self-images then do not always occur. Definition will then be much lower. For the fractional plane, the maximum trap depth and scattering rate are determined to be 1.57μK and 0.06Hz. Compared to the case of the revival plane in figure 27, both quantities are reduced despite being closer to the pattern. Such a plane is then not suitable for trapping. Again, compared to the revival example, the distribution is much more chaotic and would make it more difficult to implement accurate trapping locations.

5.3.3 Hexagonal array

Hexagonal arrays are more interesting than simple square arrays, but the Talbot effect is very similar and so only a few results need be analysed for comparison. An illustration of a particular hexagonal array, with $\frac{a}{\lambda}$ equal to 4, can be seen in figure 29a. Observing the markers for the Talbot lengths in (**b**), (**c**) represents a fractional Talbot plane. A much clearer distribution is obtained here, compared to the fractional plane of the square array in figure 28, because wave incidence here is normal to the pattern. Talbot length approximations in (**b**) are also not suitable for this simulation as both crosses are located around trap minimum. As a result of the a to λ ratio, full revivals are not technically observed. Calculations then may not necessarily align with intensity maximum. Clearly from (**c**), the fractional plane looks relatively focussed and so there is not a huge deviation from the Talbot length approximations. The maximum trap depth and scattering rate for this plane are given by 1.24μK and 0.04Hz. Being comparable

to the fractional plane of the square array in figure 28, the plane here is at a much further diffraction plane. Referring to the discussion on the Montgomery effect, the points making up each hexagonal cell lie on a circle. When revivals then occur, more points contribute to the diffraction pattern than the square. Relative intensity at the diffraction planes is then increased. An additional improvement for the hexagon is that the distribution had increased definition and sparsity. More appropriate trapping conditions may then be possible.

Far-field diffraction can also be observed with these simulations, illustrated in figure 30. For these lattice parameters, at this propagation plane, the diffraction effect changes dramatically. Rather than generating an image of the respective lattice, a magnified copy of a single unit cell is recovered. When considering trapping, this has important consequences as the structure of the trap is modified. An interesting point can be made here. Maximum trapping depths and scattering rates at this far-field region are found to be 0.85μK and 0.03Hz for the centre position. Not only this, but the outer regions of the hexagon correspond to 0.24μK and 0.01Hz. It may be hard to trap atoms at this relatively large distance, with accurate trapping positions. Within a region of 20μm, the trapping potential can be adjusted for cold atom experiments simply by changing the propagation distance. A single pattern can then be used universally.

5.3.4 Quasi-periodic array

Considering figure 31a, this choice of N means the Penrose pattern is very sparse. As a result of this, illustrated in figure 31b, the intensity drops off very quickly with propagation from the mask. It would be assumed then that this is not suitable for trapping. Analysing figure 31c gives a different proposition. A single region of concentrated intensity present at the centre of the distribution, due to only the centre holes being illuminated by the majority of the beam, could correspond to a potential trapping site. This is supported further when considering the trap depth and scattering rates. For this concentrated region, these are approximately given by 2.94μK and 0.16Hz. While the trap depth could be improved for a region that is quite close to the mask, this plane highlights the potential application of such a pattern to cold atom trapping. A more intense laser could provide a trapping lattice with the central point. These surrounding locations may then provide additional sites. Increasing the beam waist to encompass these outside points would achieve a similar result.

Figure 32 illustrates the trapping opportunity for a far more intricate quasi-periodic structure, shown in (**a**). In (**b**) the intensity is a much more jagged structure, corresponding to intense partial revivals arising as a result of increasing the number of scattering points. An example of such a plane is shown in figure 32**c**. For this 2.75μm plane, the trapping depth corresponds to the sharp peak apparent in (**b**), an example of a complex structure possibly capable of trapping cold atoms. Analysis can again be performed for two sections of the distribution. At the centre region, the trapping depth and scattering rate correspond to about 2200μK and 118Hz. For cold atom applications this is a significant trap depth, due to being in close proximity to the surface with a large hole density. A corresponding increase in the scattering rate, however, does arise as a result of the high intensity in this region (consider the intensity dependence of (5 and 4). It would be advantageous at this plane to increase detuning of the laser from atomic resonance to reduce this scattering rate. Trap depth will be negatively impacted, but the scattering rate decreases faster with detuning. A suitable

combination of trap depth and scattering rate would then maintained. At the intense regions around the centre, the trap depth and scattering rates correspond to approximately 906μK and 49.30Hz respectively. Again, this is a decent trap depth but the scattering rate remains high. A similar approach of increasing the detuning could then be implemented.

Figure 32(d) shows the resulting distribution at a more distant plane of 10.9μm, again coinciding with a peak in (b). The distribution here illustrates how the Penrose pattern can form different, yet still intricate, structures. At this plane the maximum trap depth and scattering rates are given by 544μm and 29.58Hz. Additionally, the positions around the centre in (d) correspond to 217μK and 11.8Hz. Similar approaches can be undertaken to reduce the scattering rate. The Penrose pattern can then be a very interesting component to achieve a variety of different trapping geometries. An important point to remember is that the potential landscape must be suitable for trapping, in that there are clear locations for this to occur. Trapping possibilities at other diffraction planes are then limited.

Similar to previous analysis, effects of the angle of incidence on the Penrose pattern has been investigated, shown in figure 33. Both images correspond to the same planes analysed in figure 32. The effect of this propagation direction will not be investigated in great detail, as it is expected to behave in a similar fashion to the other patterns, Clearly, however, the distribution changes drastically with this angle of incidence. To generate predictable trapping geometries it would then be imperative to ensure accurate determination of the propagation direction.

An important point to consider with the Penrose pattern, when trapping, is that the hot-spot regions can be very sparse. While typically very high in intensity, this is disadvantageous if intricate trapping distributions are desired. Importance is then placed on finding an appropriate balance between intricacy and suitable trapping depths. Pattens such as these could possess the ability to more efficiently probe atomic samples. At this stage, it is uncertain how much the effect the fringes around these hot-spot would have on efficient probing.

6 Future Developments

6.1 Holographic microscopy

Holographic imaging of cold atoms has previously been proposed for precise phase imaging of dense atomic gases, in addition to optical lattices with multiple single-state occupancies. Support for this statement is maintained after the experiments undertaken in this thesis, despite the lack of success with the high NA system alongside speckle assisted holography. Using the numerous improvement suggested in this thesis, with the current small successes, the technique should improve to a point where it can be used for imaging of complex cold atom ensembles.

Integration in cold atom experiments with atom chips should also be possible. Additional calibrations could be implemented, along with a method of retrieving the complex wavefront. During the experiment, the NA improved during its development. Potentially, this could reach quite high values (up to 0.9), meaning one can obtain higher resolutions (recall equations 30 and 31). Lens aberrations will continue to be corrected for during image reconstruction,

using Zernike functions. Based on the results presented in this thesis, however, different techniques and application of used techniques may be more suitable for aberration corrections. Combinations of these functions then may allow much improved holographic reconstruction, then applied to cold atom experiments. Despite the lack of success with using speckles for correcting aberrations, the research in this thesis and the images reconstructed present a first step in using speckles to assist in the removal of the twin image noise in digital holography.

6.2 Talbot and Montgomery simulations

Experimental investigation of Talbot/Montgomery trapping would hold many differences to simulations. For example, there will be power losses at different points of the optics and laser system such as fibre coupling. To minimize power loss, this thesis proposes to use a power recycling cavity for experiments involving a 45 degree incident beam. The simulations presented here also use the ASM that, as already explained in 5.3.1, is a scalar wave approximation and ignores the time dependence and vector nature of the electromagnetic waves. For simulations with holes, where the majority of the beam is blocked, this will have a significant impact. Work carried out in this thesis has assumed that the wave is completely blocked by the mask, but in reality there will be some transmission in the form of evanescent waves. This will affect the resulting diffraction pattern. Disk-like scatterers will reduce this effect, due to the reduced blocking of the wave, but will not eliminate it completely. Future improvements could be made by simulating this time and vector dependence. A possible method of achieving this would be with the finite different time domain (FDTD) method.

Using the simulation results, an experimental realisation of Talbot/Montgomery trapping may indeed be possible. Applications of such a trap is not immediately clear, and at this stage may not be a good use of resources considering other studies in cold atom physics. It should also be noted that the size of the spots were on the order of a micron, so an imaging method with sub-micron resolution would be ideal. An advantage may extend from the ease in formation of quasi-periodic lattices, which currently use more involved methods. Investigations into this effect may also pick up interesting physics that the rapid development of the cold atom field has left behind. Ignition of new sub-fields for exploration may then ensue. Such an example is the simulation of Anderson localization, initially an effect for describing electron localization inside a semiconductor. Using the potentials formed by a Penrose pattern, as simulated, may be a potential alleyway into exploring Anderson localization. In fact, studying a concept such as Anderson localisation may be easier than atomic trapping, since the atom only would need the quasi-crystal potential landscape of the Penrose pattern, not the additional requirement of a sufficient trap depth. New opportunities for simulations of condensed matter concepts with cold atoms may then be possible.

6.3 Holography and Penrose trapping

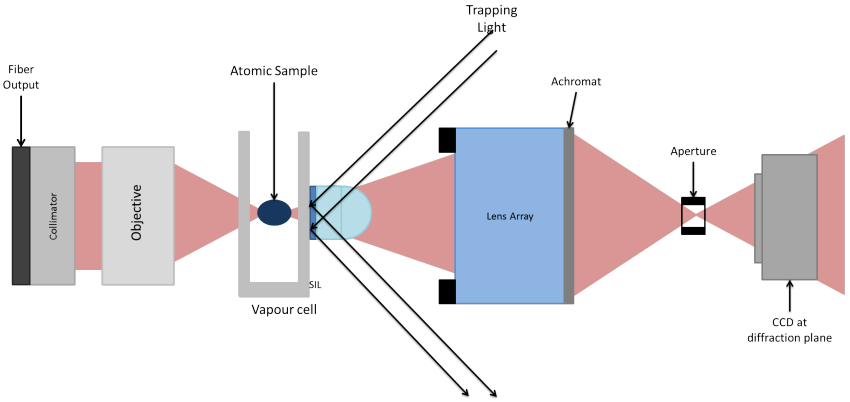

Figure 36: Proposed set-up for the combination of holographic microscopy with Talbot/Montgomery traps. This is similar to the current set-up, but would include a vapour cell for the containment of the atoms, while the additional trapping light at 45 degrees incidence provided the trapping regime. The patterns currently being used would form known speckle noises for the correction of aberrations.

An ultimate goal of this work would be to combine the imaging technique of holographic microscopy with Talbot/ Montgomery trapping. Of particular interest is the imaging of atoms in Penrose traps. Looking towards this goal, a proposed set-up is envisaged in figure 36. Similar to the current experiment in figure 14, the proposed set-up includes a vapour cell for containment of the atoms. Imaging and trapping light is also combined. Trapping light is at 45 degrees to the pattern, whereas the imaging light has normal incidence, to minimise the interaction between the two. Total internal reflection also then reduces transmission through the disks, and would also help to improve the image reconstruction through holography. Similar to performed in this theses, the disks would act as known speckle sources and enable aberration corrections. Penrose traps could then be formed in the vapour cell, allowing trapping and imaging of cold atoms. Future investigations with this set-up could pave the way for a combination of higher accuracy imaging and intricate optical lattices.

7 Conclusions

This thesis has presented techniques that can be implemented to improve holographic microscopy, using a solid immersion system for higher NA, and optimizing reconstructed images with the ERGS algorithm and Zernike functions. In addition to these improvements, an alternative method of forming cold atom lattices, using the Talbot and Montgomery effects has been investigated. This trapping has been shown to generate a variety of patterns, including the Penrose pattern, potentially allowing the formation of unique cold atom traps. Simulations have been only approximations of expected realistic effects, due to assumptions made in the associated algorithms. The wavefront reconstructed should provide a stepping stone to using the speckles for twin image removal. Aberration and noise correction was not accomplished,

but explorations and suggestions noted in this thesis will be springboards for further perfecting the technique. Another major limitation for the further future is the lack of real time imaging. Nevertheless, the authors believe that this research may bolster the interest in holographic microscopy, eventually driving it to retrieve 3D information at single atom sensitivity and contribute to the development of technology which will permit the in-situ imaging of cold atom experiments.

Appendices

A Tools for cold atom imaging

This section explains a couple of the tools often used/considered in this thesis', which may not be as well known in the cold atom or wider scientific community.

A.0.1 Solid immersion

An important concept in imaging techniques is the numerical aperture (NA), quantifying the amount of light that an imaging system can collect. It is a determining factor in the limiting resolution. Resolution can be theoretically calculated from

$$R = \frac{\lambda}{2NA}, \tag{59}$$

where the NA is defined by $NA = n \sin \mu$. Here, μ is half of the angular aperture as shown in figure 37. In air the resolution is limited by the refractive index ($n_{air} = 1$). Common techniques for increasing the NA of a system are water and oil immersion, where higher refractive index materials result in a smaller resolution. In cold atom experiments, however, it is desirable to avoid these substances in vacuum conditions. This can be solved using solid immersion (SI). SI incorporates a high NA solid into the object space, forming a solid immersion lens (SIL).

A particular example of a SIL is the hemispherical lens, theoretically capable of improving the resolution by a factor n_{SIL} (refractive index of the hemisphere), shown in figure (37). Including the hemisphere, for surface imaging results, in a higher refractive index due to refraction at the lens surface.

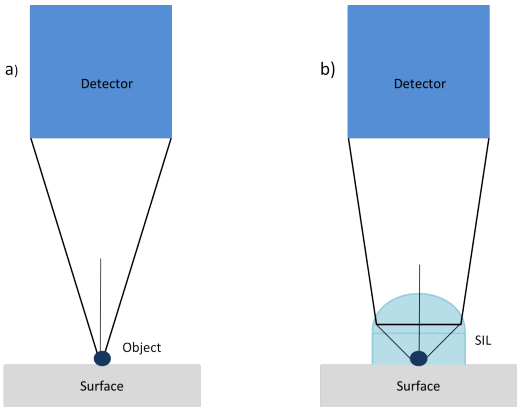

Figure 37: Comparison between the common and SIL setup for imaging of a surface object

This can also be applied to subsurface imaging, illustrated in figure 38. For a conventional imaging system, the beam would be focused below the dielectric boundary. Refraction, however, reduces the NA. This is caused by differences between the dielectric and air. Introducing

an SIL, with the same refractive index as the dielectric, circumvents theis issue by changing the planar boundary geometry. Assuming there is no interface between the dielectric material and the SIL, resolution will then be improved. Increasing μ means more light can be collected from the subsurface object.

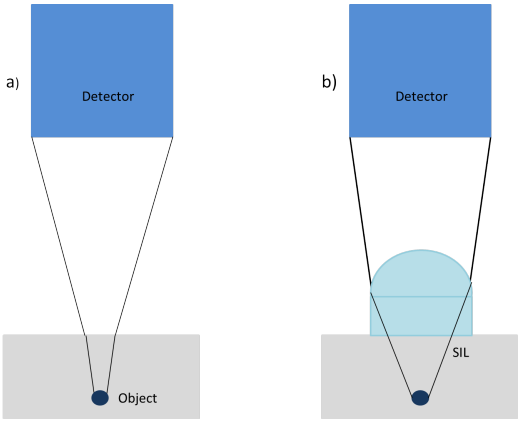

Figure 38: Comparison between the common and SIL setup for imaging of a sub-surface object

A.0.2 Acousto Optical Modulators

An Acousto Optical Modulator (AOM) is a device, typically used in cold atoms physics for:

- Fast switching of the lasers being used in the experiment,
- Fast manipulation of the frequency output of a laser beam,
- Fast manipulation of the intensity of a laser beam.

The device uses sound waves to diffract and shift the frequency of light to an integer multiple of the sound frequency. The sound waves are typically created using a piezoelectric transducer, which vibrates a crystal upon being driven. The vibration causes moving periodic planes of expansion and compression that alter the density of the crystal. This in turn alters the refractive index. A diffraction grating-like structure is then formed in the device, which creates multiple interfaces within the crystal separated by a distance λ_s. Light incident at an angle, θ, at one of these interfaces will be reflected with the same angle. A proportion of the beam will be transmitted through this first interface and the same event happens again at the next interface. The condition for constructive interference of the scattered light is known as the Bragg condition,

$$n\lambda_L = 2\Lambda sin(\theta), \tag{60}$$

where Λ is the wavelength of the incoming laser light. The frequency of the higher diffraction orders may be altered through the Doppler shift due to the motion of the interfaces. They are then shifted by an integer of the sound wave frequency.

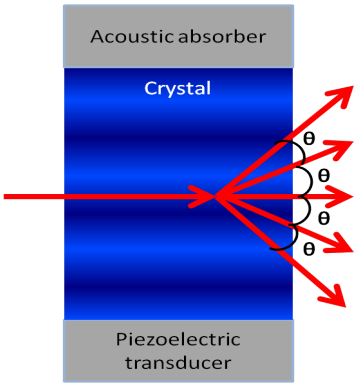

Figure 39: Schematic of an AOM showing several orders of diffraction. The sound wave at the other end of the crystal is absorbed by an acoustic absorber.

The intensity of the laser light can be simply controlled by the intensity of the sound waves by altering the input voltage to the piezoelectric vibrator. The intensity splits between the different order beams as this input voltage is altered. These devices can be used beyond cold atoms by opening experiments up for automated and fast control of any light wave - e.g. laser beams.

References

[1] Harold J Metcalf and Peter Van der Straten. *Laser cooling and trapping*. Springer Science & Business Media, 2012.

[2] John Close and Nick Robins. "Viewpoint: Precision Measurement with Cold Atoms". In: *Physics* 5 (2012), p. 26.

[3] LC Kwek and Freddy P Zen. "Quantum Information Science: An Update". In: *Journal of Physics: Conference Series*. Vol. 739. 1. IOP Publishing. 2016, p. 012001.

[4] Rudolf Grimm, Matthias Weidemüller, and Yurii B Ovchinnikov. "Optical dipole traps for neutral atoms". In: *Advances in atomic, molecular, and optical physics* 42 (2000), pp. 95–170.

[5] Yin Jian-Ping et al. "Pyramidal-hollow-beam dipole trap for alkali atoms". In: *Chinese Physics* 9.5 (2000), p. 342.

[6] CS Adams and E Riis. "Laser cooling and trapping of neutral atoms". In: *Progress in quantum electronics* 21.1 (1997), pp. 1–79.

[7] Immanuel Bloch. "Ultracold quantum gases in optical lattices". In: *Nature Physics* 1.1 (2005), pp. 23–30.

[8] M V Berry and S Klein. "Integer, fractional and fractal Talbot effects". In: *Journal of Modern Optics* 43 (10 Feb. 1996), pp. 2139–2164.

[9] John T Winthrop and C Roy Worthington. "Theory of Fresnel images. I. Plane periodic objects in monochromatic light". In: *JOSA* 55.4 (1965), pp. 373–381.

[10] Michael Dairyko et al. "On the Spectrum of the Penrose Laplacian". In: *Personal Denison* (2013).

[11] C Mennerat-Robilliard et al. "Cooling cesium atoms in a Talbot lattice". In: *EPL (Europhysics Letters)* 44.4 (1998), p. 442.

[12] Yuri B Ovchinnikov. "Coherent manipulation of atoms by copropagating laser beams". In: *Physical Review A* 73.3 (2006), p. 033404.

[13] Fu Min Huang et al. "Focusing of light by a nanohole array". In: *Applied Physics Letters* 90.9 (2007), p. 091119.

[14] RA Hull. "Transmission of light through a pile of parallel plates". In: *Proceedings of the Physical Society* 48.4 (1936), p. 574.

[15] Y Hua et al. "Talbot effect beyond the paraxial limit at optical frequencies". In: *Optics Express* 20 (13 2012), pp. 14284–14291.

[16] W B Case et al. "Realization of optical carpets in the Talbot and Talbot-Lau configurations". In: *Optics Express* 17 (23 Nov. 2009), pp. 20966–20974.

[17] W D Montgomery. "Self-Imaging Objects of Infinite Aperture". In: *Journal of the Optical Society of America* 57.6 (June 1967), pp. 772–778.

[18] F M Huang et al. "Focusing of light by a nanohole array". In: *American Institute of Physics*. series 90 (9 Mar. 2007).

[19] A Lord, K Ramakrishnan, and S Ranganathan. "An algorithm for generating quasiperiodic patterns and their approximants". In: *Bull. Mater. Sci.* 23.2 (Apr. 2000), pp. 119–123.

[20] Dennis Gabor et al. "A new microscopic principle". In: *Nature* 161.4098 (1948), pp. 777–778.

[21] WL Bragg and Gordon L Rogers. "Elimination of the unwanted image in diffraction microscopy". In: *Nature* 167.4240 (1951), pp. 190–191.

[22] Emmett N Leith and Juris Upatnieks. "Wavefront reconstruction with diffused illumination and three-dimensional objects". In: *Josa* 54.11 (1964), pp. 1295–1301.

[23] JP Sobol and Saijun Wu. "Imaging cold atoms with shot-noise and diffraction limited holography". In: *New Journal of Physics* 16.9 (2014), p. 093064.

[24] L Allen and DGC Jones. "An analysis of the granularity of scattered optical maser light". In: *Physics Letters* 7.5 (1963), pp. 321–323.

[25] David A Smith et al. "Absorption imaging of ultracold atoms on atom chips". In: *Optics express* 19.9 (2011), pp. 8471–8485.

[26] Joseph W Goodman. "Some fundamental properties of speckle". In: *JOSA* 66.11 (1976), pp. 1145–1150.

[27] TC Poon and JP Liu. *Introduction to modern digital holography with MATLAB*. New York: Cambridge University Press, 2014.

[28] JR Fienup. "Phase retrieval algorithms: a comparison". In: *Applied Optics* 21.15 (Aug. 1982), p. 2758.